


The frequency of extreme X-ray variability for radio-quiet quasars

John D. Timlin, III ^{1,2}★ W. N. Brandt,^{1,2,3} S. Zhu,^{1,2} H. Liu,^{4,5} B. Luo^{4,5} and Q. Ni^{1,2}

¹Department of Astronomy and Astrophysics, The Pennsylvania State University, 525 Davey Lab, University Park, PA 16802, USA

²Institute for Gravitation and the Cosmos, The Pennsylvania State University, University Park, PA 16802, USA

³Department of Physics, The Pennsylvania State University, 104 Davey Lab, University Park, PA 16802, USA

⁴School of Astronomy and Space Science, Nanjing University, Nanjing, Jiangsu 210093, China

⁵Key Laboratory of Modern Astronomy and Astrophysics (Nanjing University), Ministry of Education, Nanjing, Jiangsu 210093, China

Accepted 2020 August 27. Received 2020 August 27; in original form 2020 July 14

ABSTRACT

We analyse 1598 serendipitous *Chandra* X-ray observations of 462 radio-quiet quasars to constrain the frequency of extreme amplitude X-ray variability that is intrinsic to the quasar corona and innermost accretion flow. The quasars in this investigation are all spectroscopically confirmed, optically bright ($m_i \leq 20.2$), and contain no identifiable broad absorption lines in their optical/ultraviolet spectra. This sample includes quasars spanning $z \approx 0.1$ –4 and probes X-ray variability on time-scales of up to ≈ 12 rest-frame years. Variability amplitudes are computed between every epoch of observation for each quasar and are analysed as a function of time-scale and luminosity. The tail-heavy distributions of variability amplitudes at all time-scales indicate that extreme X-ray variations are driven by an additional physical mechanism and not just typical random fluctuations of the coronal emission. Similarly, extreme X-ray variations of low-luminosity quasars seem to be driven by an additional physical mechanism, whereas high-luminosity quasars seem more consistent with random fluctuations. The amplitude at which an X-ray variability event can be considered extreme is quantified for different time-scales and luminosities. Extreme X-ray variations occur more frequently at long time-scales ($\Delta t \gtrsim 300$ d) than at shorter time-scales and in low-luminosity quasars compared to high-luminosity quasars over a similar time-scale. A binomial analysis indicates that extreme intrinsic X-ray variations are rare, with a maximum occurrence rate of < 2.4 per cent of observations. Finally, we present X-ray variability and basic optical emission-line properties of three archival quasars that have been newly discovered to exhibit extreme X-ray variability.

Key words: galaxies: active – quasars: general – X-rays: galaxies – X-rays: general.

1 INTRODUCTION

Encircling the supermassive black hole (SMBH) and inner accretion disc at the centre of quasars and active galactic nuclei (AGNs) is a ‘corona’ of hot gas in which thermal UV photons are reprocessed into X-ray photons through Compton up-scattering (e.g. Galeev, Rosner & Vaiana 1979; Haardt & Maraschi 1991; Jiang, Stone & Davis 2014). Much of the emitted X-ray radiation generated by this process is directly observed as the power-law continuum in the quasar X-ray spectrum (e.g. Mushotzky, Done & Pounds 1993; Reynolds & Nowak 2003). This intrinsic X-ray emission is found to be ubiquitous in quasars (e.g. Gibson, Brandt & Schneider 2008; Pu et al., submitted); however, the basic nature and physical properties of this corona remain uncertain. Understanding the observable properties of the intrinsic X-ray emission in quasars will help to constrain further models of the corona and innermost accretion flow.

Variability of the X-ray emission from AGN is a useful probe of the underlying nature of the coronal region. For example, by measuring the characteristic time-scales of X-ray variability, McHardy et al. (2006) demonstrated that the accretion process of the SMBH in AGN has similarities to that of smaller black holes. Moreover, the observed red-noise-like X-ray power spectrum in AGN resembles that of X-

ray binaries, suggesting that a similar physical mechanism in these two classes of objects produces the X-ray photons (e.g. Green, McHardy & Lehto 1993; Uttley, McHardy & Papadakis 2002). X-ray variability from AGN has been observed over a wide range of time-scales from hours (e.g. Ponti et al. 2012) to years (e.g. Vagnetti, Turriziani & Trevese 2011; Gibson & Brandt 2012; Shemmer et al. 2017). These time-scales have been used to understand better the properties of the corona. For example, the short-time-scale variations indicate that the corona is centrally located near the SMBH (e.g. Mushotzky et al. 1993).

The amplitude of X-ray variability is another useful characterization of the underlying physics in the corona. Large-scale investigations of quasars have found that the amplitude of X-ray variability intrinsic to the quasar corona and innermost accretion flow generally increase with increasing time-scale, yet, typically does not exceed a factor of ≈ 2 (e.g. Gibson & Brandt 2012; Middei et al. 2017). In some rare cases, there have been AGNs that have exhibited extreme X-ray variations, which are often defined as variations in the X-ray flux by a factor of 10 or more. These large-amplitude fluctuations, however, are not always generated by variations in the coronal region.

External effects have sometimes been linked to extreme X-ray variability in different quasar populations. For example, X-ray variations in quasars that contain broad absorption lines (BALs) in their UV spectra have been linked to changes in the column density

* E-mail: jxt811@psu.edu

of the obscuring material along the observer’s line of sight. In this case, absorption of the X-ray photons is responsible for the observed variability (e.g. Gallagher et al. 2002; Gibson et al. 2009; Saez et al. 2012; Giustini 2016). The X-ray absorption in BAL quasars has been attributed to gas in the large-scale outflows as well as stalled ‘shielding’ gas closer to the SMBH. Additionally, X-ray variations of radio-loud quasars are often associated with variations of the jet-linked X-ray component instead of coronal variations (e.g. Carnerero et al. 2017). While these objects provide information about the nature of the quasar environment, they generally do not grant robust insight into the intrinsic variations of the quasar corona and innermost accretion flow.

There is a small subset of non-BAL, radio-quiet AGNs that also exhibit extreme X-ray variations intrinsic to the corona and innermost accretion flow, many of which are identified as narrow-line Seyfert 1 galaxies with low-to-moderate luminosity and black hole mass. One notable example is the low- z , changing-look AGN IES 192+654 that was recently discovered to have undergone an extreme X-ray variation (Ricci et al. 2020). This variation was attributed to the destruction and re-creation of the inner accretion disc and corona, perhaps by interactions between the accretion disc and debris from a tidally disrupted star. Extreme X-ray variations in higher luminosity quasars are seemingly much more rare, where only eight such objects have been confirmed to exhibit extreme X-ray variations over the past 20 yr (e.g. Strotjohann et al. 2016; Liu et al. 2019; Ni et al. 2020). A loose constraint on the rate of intrinsic extreme X-ray variability in quasars was briefly estimated as part the analysis of Gibson & Brandt (2012), which investigated the general X-ray variability properties of spectroscopically confirmed quasars; however, both the small sample size and the presence of X-ray upper limits in the sample affected the statistical power of their constraint. Two of the eight quasars were recently found to vary in X-ray flux by more than a factor of 10 (SDSS J0751+2914, Liu et al. 2019; SDSS J1539+3954, Ni et al. 2020). Given the apparent rarity of these extreme events, it was somewhat surprising that these two events were found at nearly the same time. A larger-scale systematic investigation is therefore warranted in order to understand better the frequency of these extreme variations.

In this investigation, we aim to constrain better the frequency of extreme X-ray variability that is intrinsic to the quasar corona or due to other changes in the central accretion flow (hereafter, we will refer to the combination of these two phenomena as intrinsic X-ray variability). Such intrinsic variability could be due to changes in the coronal emission or due to X-ray absorption by a thick inner accretion disc as in the case for quasars with weak emission lines and quasars with high Eddington ratio (e.g. Luo et al. 2015; Liu et al. 2019; Ni et al. 2020). To constrain better this frequency, we assembled a large, unbiased sample of radio-quiet quasars that are devoid of BALs and have multiple, high-quality X-ray measurements. This large sample provides a sufficient number of quasars to more tightly constrain the frequency of intrinsic extreme X-ray variability. Studying the occurrence rate of extreme X-ray variation of the innermost accretion flow provides insight into the nature of the corona and thus will help inform physical models of the X-ray emission from typical quasars in general.

This paper is organized as follows: Section 2 describes the data sets used to assemble a sample of typical quasars for this investigation and presents the methods used to find X-ray counterparts. The data-analysis techniques used to reduce and analyse the X-ray data are discussed in Section 3. Section 4 presents the variation of quasars over time, presents the frequency of extreme X-ray variability among typical quasars, and discusses the implications of these results. Serendipitously discovered extremely X-ray variable quasars are

presented in Section 5, and our results are summarized in Section 6. Throughout this work, we adopt a flat Λ -CDM cosmology with $H_0 = 70 \text{ km s}^{-1} \text{ Mpc}^{-1}$, $\Omega_M = 0.3$, and $\Omega_\Lambda = 0.7$, and we utilize the CIAO (Chandra Interactive Analysis of Observations; Fruscione et al. 2006) version 4.10¹ software and CALDB version 4.8.3.²

2 SAMPLE SELECTION

To assemble our quasar catalogue, we combined the SDSS data release fourteenth quasar catalogue (DR14Q; Pâris et al. 2018) and the large quasar catalogue from Richards et al. (2015) which compiled other spectroscopically confirmed quasars that overlap the SDSS imaging footprint. A brief description of these two survey catalogues is given below along with the method used to find serendipitous, multi-epoch *Chandra* observations. We also describe the methods used to flag and remove quasars that have BALs or strong radio emission.

2.1 Optical data

The SDSS DR14Q (Pâris et al. 2018) catalogue compiled optical properties of all 526 356 quasars that were observed in the first three SDSS projects (York et al. 2000; Eisenstein et al. 2011) as well as the first data release of the fourth SDSS project (Dawson et al. 2016). In total, DR14Q contains quasars over an area of $\approx 9376 \text{ deg}^2$ across the sky that span a wide redshift range, the majority of which are between $0.1 \leq z \leq 4$. The redshifts reported in the catalogue have been either visually measured or obtained using a principal component analysis (PCA) on the source spectrum (e.g.; Pâris et al. 2012). Also included is a measurement of the balnicity index (BI_CIV; Weymann et al. 1991), which indicates the presence of a BAL near the CIV emission line. Additionally, the quasars in the DR14Q catalogue have been matched to the objects detected in the Faint Images of the Radio Sky at Twenty centimeters (FIRST; Becker, White & Helfand 1995) survey and the radio fluxes have been recorded for matching quasars. Analysis of the frequency of extreme X-ray variability for typical quasars requires that the X-ray counterparts be almost always detected; therefore, we also impose an empirically determined restriction on the apparent magnitude of $i \leq 20.2$ because optically bright quasars tend also to be brighter in X-rays. This sample contains 222 358 total quasars.

To the DR14 quasar catalogue, we added quasars from the comprehensive quasar catalogue presented in Richards et al. (2015). This catalogue mainly contains quasars from SDSS-I/II/III (York et al. 2000; Eisenstein et al. 2011) through data release 10 (DR10) and thus, these quasars are reported in the DR14Q catalogue; however, it also includes spectroscopically confirmed quasars from the 2dF quasar redshift survey (2QZ; Croom et al. 2004), the 2SLAQ survey (Croom et al. 2009), and the AGES project (Kochanek et al. 2012) that lie within the SDSS footprint but have no SDSS spectrum. For each quasar in this comprehensive catalogue, Richards et al. (2015) reported the photometric information from SDSS, along with the redshift measurements from the respective survey, which allows us to straightforwardly combine these data with the information from the DR14Q catalogue. Imposing the same i -band magnitude cut as before, this catalogue returns an additional 21 669 quasars not reported in the DR14Q catalogue. Although the Richards et al. (2015) quasar catalogue adds a relatively small number of quasars

¹http://cxc.harvard.edu/ciao/releasenotes/ciao_4.10_release.html

²<http://cxc.harvard.edu/caldb/>

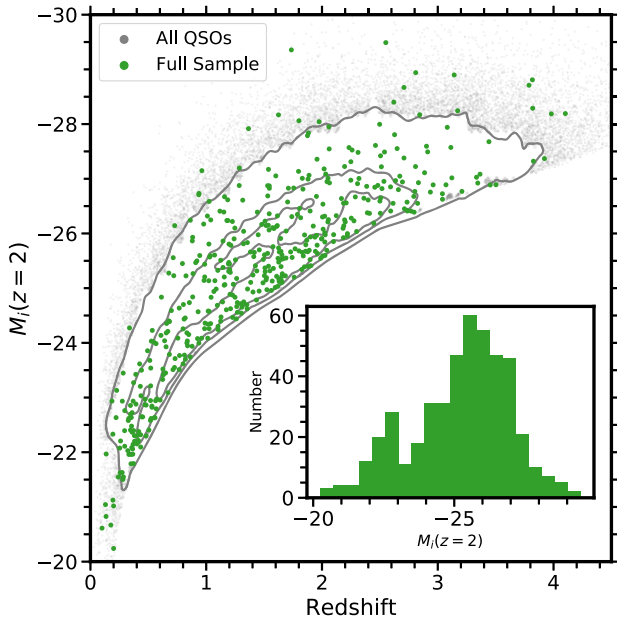


Figure 1. Absolute i -band magnitude (corrected to $z = 2$; Richards et al. 2006) as a function of redshift for all of the confirmed quasars that were used to search for serendipitous *Chandra* observations. The grey contours enclose 35, 68, and 95 per cent of the quasars. The green points depict the quasars in our Full sample that have multiple, high-quality *Chandra* X-ray observations as described in Section 3.3. The inset plot shows the M_i distribution of the quasars in the Full sample.

compared to the DR14Q sample, our scientific goal of constraining the frequency of extreme X-ray variability requires as many quasars as possible; therefore, we elected to retain these objects in our analysis.

In total, we obtained 244 027 bright quasars that we used to search the *Chandra* data base for serendipitous observations. The quasars assembled from the aforementioned catalogues form a reasonably homogeneous combination of typical, blue type-I quasars. We depict the absolute magnitude of the quasars in this sample as a function of their redshift in Fig. 1. Even after imposing a restriction on the apparent brightness, this full quasar sample spans a wide range in luminosity and redshift.

2.2 Finding *Chandra* counterparts

In this investigation, we elected to perform X-ray photometry of the SDSS quasars in the *Chandra* events files rather than simply match these quasars to the *Chandra* Source Catalogue (CSC; Evans et al. 2010). Performing the analysis in this manner allows us to examine these quasars to a greater sensitivity than would be provided by a simple match to the blind-search CSC and it enables us to generate optimal constraints on quasars that are not detected. We closely followed the methods described in Timlin et al. (2020) to search for serendipitous counterparts in the *Chandra* data, which will be outlined below. Restricting our analysis to only the serendipitously observed sources removes any potential biases that might arise due to the exceptional properties of targeted quasars. In this work, we only consider *Chandra* observations through MJD = 58 504 (2019 January 21), which includes 7122 *Chandra* observations used in the analysis. Our scientific results could be heavily affected by the presence of X-ray non-detections in the sample (see Section 4.1); therefore, we only considered observations from *Chandra* as op-

posed to other observatories (e.g. *XMM-Newton*) because its low point-source background levels make it well suited to detecting serendipitous objects. *Chandra* has been taking high-quality data for ≈ 20 yr which enables us to probe quasar variability on time-scales that span a significant fraction of a human lifetime.

As in Timlin et al. (2020), we began searching for serendipitous counterparts using the Multi-Order Coverage (MOC³) map, which approximates the regions of the public *Chandra* observation footprints, to quickly remove quasars in our large sample that are not covered by a *Chandra* observation. Next, the CIAO (Fruscione et al. 2006) tool `find_chandra_obsid` was used to find the observation ID associated with the given position of a quasar; we searched only for detections with the ACIS instrument (Garmire et al. 2003) where no gratings were used in the observation. We retained all observations of any given quasar regardless of how many times it was observed. Quasars were required to lie no less than 30 pixels (≈ 15 arcsec) from the edge of a detector to remove non-detections and low-quality measurements due to the quasar lying partially outside of the detector.

In total, we found 12 283 *Chandra* observations of 7813 quasars that passed the above criteria. For the purpose of this investigation, we were only interested in keeping quasars that had more than one observation in order to compute the variation between the epochs. After removing observations with only a single epoch of observation, 4035 observations of 1160 quasars remained. Quasars with off-axis angles < 0.5 arcmin were removed to ensure that the X-ray coverage was serendipitous. Additionally, since the point spread function (PSF) size and vignetting effects increase at large off-axis angles, we also required that our sample lie within 9 arcmin of *Chandra* pointing positions, which restricted our sample to 3155 observations of 878 quasars. We depict the distribution of the number of *Chandra* observations per quasar for this sample of 878 quasars in Fig. 2. The majority of quasars that were found serendipitously have fewer than five *Chandra* observations.

3 MULTIWAVELENGTH DATA ANALYSIS

3.1 X-ray data reduction

Each of the aforementioned observations was processed using standard CIAO tools (Fruscione et al. 2006), again closely following the method detailed in Timlin et al. (2020). The primary and secondary data files were used to generate a bad pixel file, an event list, and a spectrum file using the `chandra_repro` tool. A background cleaning procedure was also implemented in this step and is dependent on the observation mode of the ACIS camera. Background flares were then removed using the `deflare` tool, which flags the MJD of any spurious counts above the 3σ level.

From the flare-filtered, reprocessed events files, a full-band (0.5–7 keV), a soft-band (0.5–2 keV), and a hard-band (2–7 keV) image were created using the `dmcopy` tool (using ASCA grades 0, 2, 3, 4, 6) for each observation. Sources were extracted from each of the three images using the `wavdetect` tool with a false-detection probability of 10^{-6} . The X-ray positions of the detected sources in each image were combined to form a complete detection list and the optically determined position of the quasar was matched to this list. If the quasar position matched within 2 arcsec of the X-ray position of a source in the list, the X-ray position from `wavdetect` was adopted; otherwise, photometry was performed on the X-ray image at the optically determined position of the quasar.

³http://cxc.cfa.harvard.edu/cda/cda_moc.html

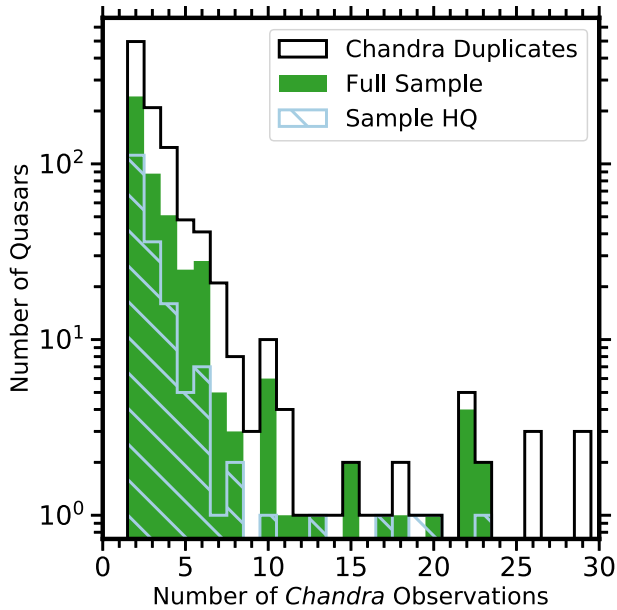


Figure 2. The number of serendipitous *Chandra* observations that comprise the X-ray light curve for each of the quasars in our samples. The open black histogram depicts the initial sample of 878 quasars with multiple *Chandra* observations that were assembled in Section 2. The green and blue hatched histograms show the number of *Chandra* observations of the quasars in our Full sample and Sample HQ (which has a 100 per cent X-ray detection fraction), respectively, as defined in Section 3.3. We find that most quasars have been serendipitously observed between two and five times with *Chandra*, however, there are cases where *Chandra* has serendipitously observed the same quasar ≥ 10 times.

Counts were extracted at the source position using a matched-filter region instead of the circular regions used in Timlin et al. (2020). While circular regions are a simple and effective aperture to use for positions near the aim-point, as the off-axis angle increases the size of the circle must also increase to surround the majority of the counts, which leads to a larger number of background counts being enclosed by the source region. The matched-filter technique instead used the best-fitting elliptical region of a simulated source at the same position on the ACIS chip as the quasar. This method removes the excess background enclosed by a circular region, thus improving the sensitivity of the source detection.

Sources were simulated using the MARX (Model of AXAF Response to X-rays; Davis et al. 2012) software suite. MARX is a ray tracing programme that is designed to simulate realistic observations with the *Chandra* telescope considering the true properties of an observation (e.g. MJD, detector ID, nominal pointing information, source location, the aspect solution file, and a real or simulated spectrum). MARX was run for each of the three energy-dependent images that were created for every observation. The MARX suite creates an image of the simulated photons similar to the observation data files for a user-defined exposure time. The `dmellipse` tool was used to fit an elliptical region that enclosed 90 per cent of the simulated photons and was subsequently used to extract counts from the observation. All of the regions were visually inspected to ensure that the fitting procedure succeeded in describing the simulated images and that the regions were sensible to use for extracting counts in the observed image.

Background counts were extracted using circular annuli with inner (outer) radii of 15 (50) arcsec surrounding the source position. If there is a source detected by `wavdetect` that overlaps this region,

we subtract the contribution of the elliptical region provided by `wavdetect` from the total background. Additionally, we remove the sections of the background region that fall off the chip boundary, forming a ‘pie’-shaped region (e.g. Pu et al., submitted). This method systematically defined the background regions that best described the local background near the source. All of these background regions were visually inspected. In a small number of cases when the quasar had many neighbors, we placed a circular background region in a nearby, source-free location for a more appropriate measurement of the background.

Exposure maps were created using the `flux_image` tool to quantify the effective exposure at the off-axis position of the quasar (the exposure maps generated in this work have units of photons $^{-1}$ cm 2 s). Additionally, the `flux_image` tool incorporates the decline of the ACIS quantum efficiency over time into each exposure map. Effective exposure time, which is the exposure time corrected for this loss of sensitivity, was computed by multiplying the exposure time of the observation by the ratio of the median value from the exposure map in the source region to the maximum value of the exposure map. This ratio represents the vignetting effects at the source position compared to that of an on-axis observation. We use the median value of the exposure map in the source region to reduce the effect of individual bad pixels within the source region. Exposure maps were created for each band using effective energies of 1, 3, and 2 keV for the soft, hard, and full band, respectively.⁴ The exposure maps were input into the `dmextract` routine when extracting counts files from each of the three energy bands.

The source detection significance for each band was computed using the binomial no-source probability (e.g. Broos et al. 2007; Xue et al. 2011; Luo et al. 2015), P_B , using the formula

$$P_B(X \geq S) = \sum_{X=S}^N \frac{N!}{X!(N-X)!} p^X (1-p)^{(N-X)}, \quad (1)$$

where S is the total source counts, N is the total number of raw source and background counts, and $p = 1/(1 + f_{\text{area}})$, where f_{area} is the ratio of the background to source region area. Since we are performing forced-photometry at the pre-specified positions of optically bright objects, we consider a source to be detected if $P_B \leq 0.02$ (2.3σ), and calculate the 1σ errors on the net source counts following the numerical method of Lyons (1991) and the method described in Gehrels (1986). We find that the vast majority (≈ 96 per cent) of the quasars in this investigation have a *Chandra* detection significance of $P_B \ll 0.0001$ and thus relaxing the detection threshold to $P_B \leq 0.02$ does not introduce a large number of false positives into our analysis (see Section 3.3 for more details). When a source is not detected, we use the Poisson confidence interval method (Kraft, Burrows & Nousek 1991) to estimate a 90 per cent confidence upper limit on the counts. Finally, in this investigation, we do not compute physical flux values from the counts, but rather we elect to work with count fluxes to eliminate additional uncertainties that come from estimating physical flux (see Section 4.1).

3.2 Radio-loud and BAL quasars

The goal of this investigation is to determine the frequency of intrinsic extreme X-ray variability among the majority population of radio-

⁴We adopted effective energies similar to those presented in the `flux_image` documentation (<https://cxc.cfa.harvard.edu/ciao/ahelp/fluximage.html>). Reasonable changes in the energy were found to have little effect on the results.

quiet quasars. Radio-loud quasars have traditionally been thought to exhibit X-ray emission associated with their jets in addition to coronal emission (e.g. Miller et al. 2011; Zhu et al. 2020). We also exclude BAL quasars from our sample since their observed X-ray emission can vary due to absorption changes in the central region instead of a change in coronal emission (see Section 1). In this investigation, we flag and remove these two populations in the same manner as in Timlin et al. (2020), which we will briefly describe below.

To remove radio-loud quasars from our sample, we compute the radio-loudness parameter, $R = f_{6\text{cm}}/f_{2500}$, where $f_{6\text{cm}}$ and f_{2500} are the quasar fluxes at rest frame 6 cm and 2500 Å, respectively (Kellermann et al. 1989). We convert the apparent i -band magnitude into the 2500 Å flux following the method in Section 5 of Richards et al. (2006). The rest frame 6 cm flux is computed using the 20 cm flux (assuming a radio spectral index of $\alpha_\nu = -0.5$) from the Faint Images of the Radio Sky at Twenty-Centimeters (FIRST; Becker et al. 1995) survey or the NRAO VLA Sky Survey (NVSS; Condon et al. 1998) data base if the quasar is not covered by FIRST. For quasars that are not detected at 20 cm, the 3σ upper limit on the flux was estimated as $0.25 + 3\sigma_{\text{rms}}$ mJy, where σ_{rms} is the RMS flux at the source position and 0.25 mJy is the CLEAN bias correction for the FIRST survey (White et al. 1997; the CLEAN bias correction for NVSS is 0.3).

Typically, a quasar is taken to be radio loud if $R > 10$ (e.g. Kellermann et al. 1989); however, previous investigations have found that significant X-ray contributions from the jet are not generally present until $R \gtrsim 100$ (e.g. Miller et al. 2011; Zhu et al. 2020). We find that ≈ 43 per cent of our sample has 3σ upper limits of $R \leq 10$, whereas ≈ 94 per cent of the sample has upper limits of $R \leq 30$, which is considerably lower than the R -level at which the jet generally contributes significant X-ray emission. The quasars in this sample with $R \leq 30$ can therefore realistically be considered either radio-quiet or mildly radio-intermediate. In either case, the coronal X-ray emission should be the dominant source of X-rays in these quasars; therefore, we retain quasars in our sample with $R \leq 30$. In total, 32 radio-loud objects ($R > 30$) are flagged and removed from the sample.

The balnicity index can be used for a first-cut removal of BAL quasars in the sample (e.g. removing $\text{BI}_{\text{CIV}} > 0$); however this parameter is only provided for the quasars in the DR14Q catalogue. To identify and remove BALs in our full sample, we first fit the spectrum of each quasar using the PYQSOFIT⁵ (Guo, Shen & Wang 2018) software. Following the method described in Section 3.2 of Timlin et al. (2020), we fit the global continuum of each quasar with a power-law model and the C IV and Mg II emission lines with three Gaussian profiles when they were present in the quasar spectrum. Absorption troughs were identified as the 3σ flux outliers between the data and the best-fitting model, and their width was measured as the distance between the two pixel locations where the trough intersected with the model. When the width was $\geq 2000 \text{ km s}^{-1}$, we flagged the object as a BAL quasar. At low- z ($z \leq 1.7$), the C IV emission line has shifted out of the UV spectrum, so we instead identified BALs to the lesser extent possible in the Mg II emission-line region since quasars with Mg II BALs almost always harbor C IV BALs (e.g. Zhang et al. 2010). A lack of a Mg II BAL does not necessarily demonstrate that the spectrum is devoid of BALs; however, we retain such quasars in our sample. Using the fraction of identified BALs at high-redshift and the Mg II BALs already discovered at low-redshift in our sample, we conservatively estimate that unidentified BAL quasars will comprise $\lesssim 10$ per cent of the Full sample (defined in the next Section). The number of unidentified

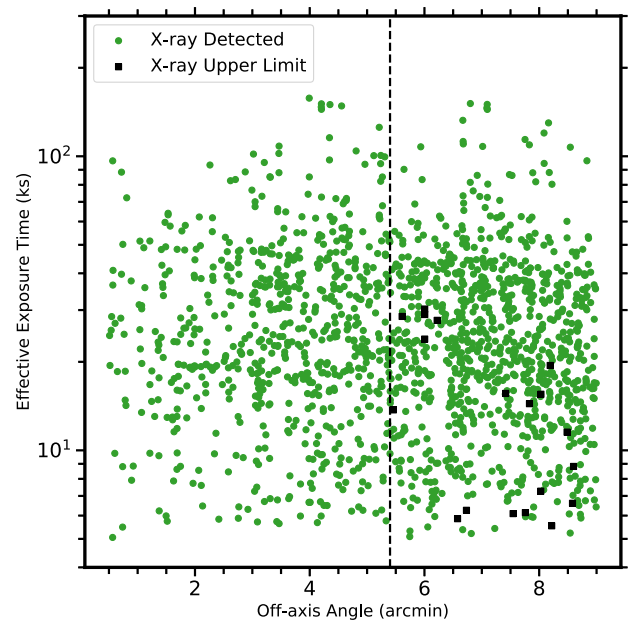


Figure 3. Effective exposure time as a function of off-axis angle for each of the 1598 *Chandra* observations in our Full sample. Green points depict observations that are X-ray detected in at least one band according to the binomial no-source probability, whereas black squares represent quasars that are not detected in any X-ray band. The vertical dashed black line shows the location of the cut to generate Sample HQ. All of the quasars with off-axis angle less than threshold (5.4 arcmin) are X-ray detected and thus the analysis of these objects in Section 4 will not be affected by X-ray upper limits.

BAL quasars that remain in our sample should be sufficiently small as to not have a large impact on the results. In total, 44 BAL quasars were robustly identified and removed from the sample.

3.3 The typical quasar sample

In addition to the initial restrictions on the data (i -band magnitude, *Chandra* MJD, and off-axis angle) as well as the removal of BAL and radio-loud quasars, some final cuts were made after the X-ray images were processed. First, quasars that overlap an ACIS chip gap were removed from the sample since the sensitivity in these regions is much lower than for the rest of the chip and can result in low-sensitivity non-detections. We also removed twenty quasars that lie near X-ray bright clusters of galaxies since the clusters can significantly and non-uniformly increase the background level in the source and background regions which lowers the sensitivity of the observation. Furthermore, we removed observations that are less sensitive by requiring that all of our quasars have an effective exposure time of at least 5 ks. Fig. 3 depicts the effective exposure time as a function of off-axis angle for the quasars considered in the work. For the small background levels in a single *Chandra* observation and off-axis angles considered in this investigation, a flat cut in effective exposure time roughly corresponds to a cut in the limiting flux of an observation. At off-axis angles larger than ≈ 9 arcmin, the PSF size and vignetting effects become very large, making the observations less sensitive.

After imposing these further criteria, 1598 high-quality observations of 462 quasars remained in the sample (hereafter the Full sample; see Table 1). We find that only 19 of the 1598 *Chandra* observations (1.1 per cent) had quasars that were X-ray undetected and thus have an upper limit on the X-ray counts. In this investigation,

⁵<https://github.com/legolason/PyQSOFit>

Table 1. Serendipitous quasar sample properties.

Sample (1)	N_Q (2)	N_{obs} (3)	f_{detected} (4)	N_{pairs} (5)	$\langle m_i \rangle$ (6)	$\langle M_i(z=2) \rangle$ (7)
Full	462	1598	0.988	2567	19.2	−25.54
Full*	462	1144	0.987	899	19.2	−25.54
HQ	185	583	1.000	818	19.3	−25.56
HQ*	185	443	1.000	331	19.3	−25.56

Basic properties of the different samples used throughout this paper. Each row provides the information for the samples considered in this work, described in Sections 2 and 3.3 (the ‘*’ indicates that the X-ray light curves have been down-sampled to three epochs using the method in Section 4.1). Columns 2 and 3 provide the total number of quasars and *Chandra* observations and column 4 records the detection fraction of the observations in column 3. Column 5 presents the number of epoch pairs in the sample (see Section 4.1) and columns 6 and 7 report the average values of the *i*-band apparent magnitude and absolute magnitude of each sample.

we consider an object to be X-ray detected if the binomial no source probability is $P_B \leq 0.02$ in any band. As mentioned in Section 3.1, the majority of the observations in the Full sample are detected with a high significance ($P_B \ll 0.0001$). Since the measurements are independent of each other, we can sum the no-source probabilities to estimate the number of false positives present in the sample. The total number of false-positive sources expected in this sample is ≈ 0.7 using $P_B \leq 0.02$ as the detection threshold.

Any X-ray upper limits in our sample could lower the statistical power of our final result; therefore, we also create a high-quality sample which has a 100 per cent X-ray detection fraction by reducing the cut in off-axis angle from 9 to 5.4 arcmin (dashed vertical line in Fig. 3). This high-quality sample (hereafter, Sample HQ; see Table 1) contains 583 *Chandra* observations of 185 quasars and will not be affected by upper limits. Both the Full sample and Sample HQ are dominated by quasars that have less than five serendipitous *Chandra* observations as shown in Fig. 2. The Full sample of quasars is available online in machine-readable format (see Appendix A for more details).

4 THE FREQUENCY OF EXTREME X-RAY VARIABILITY

4.1 The count flux ratio

We perform our analyses in terms of count flux ($\text{cts cm}^{-2} \text{s}^{-1}$) rather than physical flux ($\text{erg cm}^{-2} \text{s}^{-1}$) to remove additional uncertainty that comes from fitting a spectral model to the X-ray data. The count flux is defined as the ratio between the background-subtracted counts of each source and the average effective area at the quasar position in the exposure map (the exposure maps incorporate the off-axis effective area and quantum efficiency of the observation, and are in units of $\text{photons}^{-1} \text{cm}^2 \text{s}$). In this investigation, we use the counts in the observed-frame full band (and the respective exposure map) to compute the count flux.⁶ Uncertainties in the count flux are computed by propagating through the count errors from Section 3.1.

⁶Quasars in nine observations were not detected in the full band but instead were detected in the soft (seven quasars) or hard (two quasars) bands. In these cases, the measured counts from the full band were used to compute the count flux. All nine observations have a binomial no-source probability in the full band that is only slightly larger than the detection threshold (with a maximum value of $P_B \approx 0.04$), and thus performing forced photometry at the known source location provides a reasonable estimate of the the full-band counts.

In this investigation, we measure the amplitude of X-ray variability in the *observed*-frame full band (0.5–7 keV), where the ACIS instrument is most sensitive, instead of converting to a common rest-frame bandpass. Choosing an ideal rest-frame bandpass well suited to studying all of the quasars in the sample would be challenging since the sample spans a wide range in redshift. Creating such a rest-frame bandpass would require that, for quasars at different redshifts, the observed-frame energy range be reduced and counts be extrapolated from this smaller bandpass. This would reduce the sensitivity of the measurements by removing energies where *Chandra* is most effective for typical observations and greatly increase statistical uncertainties. Using the measurements in the observed-frame full band ensures that each observation is performed with the maximum sensitivity provided by *Chandra* which is critical in this work since our goal of constraining the frequency of extreme X-ray variability requires that the sample have a very high detection fraction. X-ray non-detections may occur for several reasons, one of which being that the quasar has varied by an extreme amplitude. Using X-ray limits to compute the amplitude of variability, which is defined in this work as the ratio of count fluxes between two time-ordered epochs (see below), yields either an upper or lower limit on the amplitude. Incorporating both upper and lower limits (left and right censored data) into some statistical tests and analysis techniques is not straightforward, and improper treatment of the limits (e.g. inappropriate assumptions about their underlying distribution) might substantially impact the outliers of the distribution. The extreme X-ray variability events are the outliers in the variability amplitude distribution; therefore, it was imperative that the most sensitive *Chandra* observations were used in order to reduce the number of X-ray limits in the sample.

Since the observed-frame bandpass probes different rest-frame energies depending on the quasar redshift, combining the variability amplitudes of different quasars presumes that different parts of the quasar X-ray spectrum vary in a basically similar manner. Previous investigations have found that the X-ray spectral slope is not highly dependent on redshift (e.g. Just et al. 2007; Green et al. 2009), which implies that a similar power-law trend should be present at the rest-frame energies that are being observed. Furthermore, investigations of individual Seyfert 1 AGN have demonstrated that the X-ray flux variations between the hard and soft bands are dominated by a change in normalization of the spectrum as opposed to different fluctuations in the bands; although, a secondary constant component was also found at hard X-ray energies, which has been associated with Compton reflection (e.g. Taylor, Uttley & McHardy 2003, Vaughan & Fabian 2004). Gibson & Brandt (2012) found evidence for this two component model in quasars as well. Using a large, heterogeneous sample of X-ray detected quasars, Serafinelli, Vagnetti & Middei (2017) found a ‘softer when brighter’ trend which may similarly indicate the existence of this two component model of X-ray variability in quasars. Their investigation also found no clear evidence that this trend depends on redshift, X-ray luminosity, black hole mass, or Eddington ratio. These previous investigations demonstrated that the X-ray variability of quasars is dominated by a constant normalization over the X-ray spectrum, in agreement with the assumption in this work; however, the secondary constant component suggests that this assumption may not be perfect and thus further investigation is required to determine the magnitude of this effect on high-energy X-ray variability. Such an investigation is outside of the scope of our work. Therefore, the results reported below should therefore be interpreted as the variability of each quasar given the available X-ray data in the observed-frame full band.

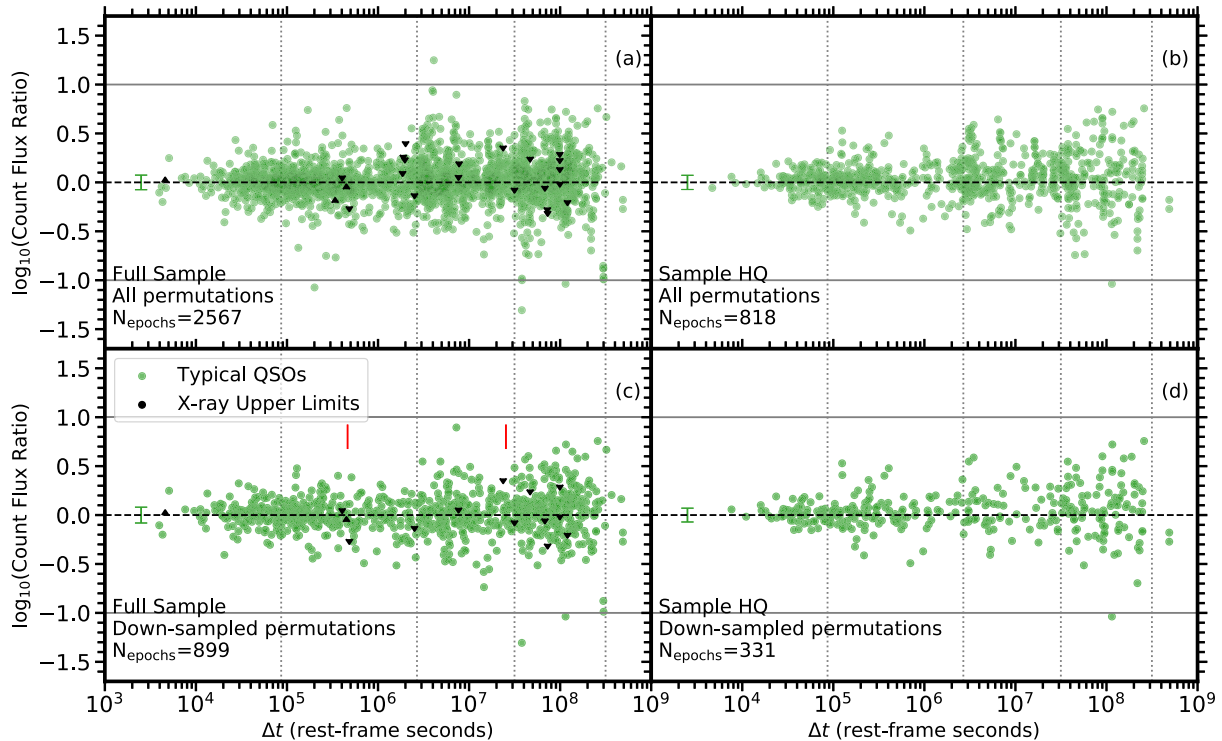


Figure 4. Count flux ratio as a function of the rest-frame time difference between two *Chandra* epochs for the quasars in each sample. Panels (a) and (b) depict this ratio for every epoch pair for all of the quasars in the Full sample and Sample HQ, respectively. We mitigate the epoch-permutation effect in panels (c) and (d) for the Full sample and Sample HQ, respectively, by only considering the earliest and latest observations along with a randomly drawn epoch in the middle. Green data points depict epoch pairs where both measurements are X-ray detected and black arrows represent when one of the measurements in a pair is an upper limit. The direction of the arrow indicates whether the X-ray limit is in the numerator (down arrow) or the denominator (up arrow) of the ratio. The black dashed line shows when the count flux ratio is unity and the two grey lines show a count flux ratio of ten. The vertical dotted lines in each panel correspond to time-scales of 1 d, 1 month, 1 yr, and 10 yr from left- to right-hand side, respectively. The error bars represent the median error of the count flux ratio in each sample and the short red vertical lines in panel (c) mark where we split the data into three time-scale bins (see Section 4.2). These panels show that X-ray variability by a factor of 10 or more is extremely rare in quasars.

The ratio of full-band count fluxes between *Chandra* epochs was used to quantify the amplitude of X-ray variability. In order to space evenly this fractional change in flux around a ratio of one (e.g. no change in flux), we used $\log_{10}(\text{count flux ratio})$ as our metric for variability. The time-scale of this variability is defined as the difference between the start times (converted to the rest frame) of the two *Chandra* observations. As shown in Fig. 2, many of the quasars in the Full sample and Sample HQ have only two epochs of *Chandra* observations, and thus have only one measurement of variability and time-scale. For quasars with more than two observations, the count flux ratio was measured between every unique pair of epochs which yield $N(N - 1)/2$ permutations of variability measurements and time-scales, where N is the number of times the quasar has been observed with *Chandra*. The number of pairs for each sample is provided in Table 1.

Quasars in the Full sample and Sample HQ with > 10 serendipitous *Chandra* observations were down-sampled such that there are only 10 observations in the X-ray light curve. This down-sampling reduced the effect of a single quasar with a large number of epoch permutations on the overall distribution of the count flux ratios (hereafter, we refer to these as the ‘All permutations’ samples). A simple unbiased down-sampling method was employed that retained only the earliest observation, the latest observation, and eight randomly selected epochs between the two. In addition to reducing the effect that any one quasar had on the sample, this method also maintained the large temporal separation between X-ray observations of each quasar. Even

after this down-sampling, these samples could still be biased by the heavy weighting of some multiply observed objects. To reduce further the effect that any single quasar had on the investigation, we again down-sampled the *Chandra* light curves of each quasar to three epochs using the same method. The count flux ratios were also computed for these two additional samples (hereafter referred to as the ‘down-sampled permutations’ samples; see Table 1).

4.2 Extreme X-ray variability and time-scale

Previous investigations of X-ray variability in quasars have found that the X-ray emission can vary on time-scales of days to years (e.g. Gibson & Brandt 2012; Vagnetti et al. 2016; Shemmer et al. 2017). In this work, we specifically seek to investigate the behaviour of extreme X-ray variations over time. We therefore examined the count flux ratio as a function of time-scale, Δt , in Fig. 4 for the epoch pairs in the Full sample (panel a; 2567 pairs) and in Sample HQ (panel b; 818 pairs), as well as the down-sampled Full sample (panel c; 899 pairs) and Sample HQ (panel d; 331 pairs). The green points depict the count flux ratio of pairs where both observations provide X-ray detections. When one observation is an X-ray upper limit, we use the 90 per cent confidence value from Section 3.1 to determine a limit on the count flux ratio (black arrows in Fig. 4). Arrows pointed down (up) represent the X-ray limit being in the numerator (denominator) in the ratio. Three epoch pairs were removed from the sample because neither observation provided an X-ray detection.

Uncertainty in the count flux ratio was computed by propagating the errors in the counts using the method from Lyons (1991; green error bars show the median uncertainty in the data set). Fig. 4 clearly shows that typical quasars do not generally vary by more than a factor of ≈ 3 ($\log_{10}(\text{count flux ratio}) \approx 0.5$) in any of our samples and that larger amplitude variations are rare.

Fig. 4 also suggests that the variability factor generally becomes larger at longer time-scales in each of the samples as suggested by previous investigations (e.g. Gibson & Brandt 2012). It is therefore more instructive to split the sample by time-scale and investigate the extreme X-ray variability properties of these sub-populations. We split the samples into short ($\Delta t \leq 0.463 \times 10^6$ s; 284 measurements), intermediate ($0.463 < \Delta t \leq 25.4 \times 10^6$ s; 297 measurements), and long ($\Delta t > 25.4 \times 10^6$ s; 318 measurements) time-scale bins of approximately equal sample size as presented in Fig. 5. The short, intermediate, and long time-scale bins roughly correspond to time-scales of $\Delta t \lesssim 5.3$ days, $5.3 \lesssim \Delta t \lesssim 294$ days, and $\Delta t \gtrsim 294$ days, with median values of 1.1 d, 61 d, and 3 yr, respectively. We only depict the count flux distribution of the Full quasar sample with the down-sampled permutations (panel c from Fig. 4) here since it maximizes the number of quasars in the sample but minimizes the effect any one quasar has on the final results.⁷ Analysing the shape and symmetry of these three distributions, as well as their similarity to each other, will provide insight into the nature of the extreme X-ray variations at short, intermediate, and long time-scales.

Previous analyses have found that the X-ray flux distribution of AGN can be generally well modelled by a lognormal distribution (e.g. Uttley, McHardy & Vaughan 2005). The product or ratio of two lognormal distributions results in a lognormal distribution, much like the sum or difference of two normal distributions returns a normal distribution. Therefore, the count flux ratio should follow a lognormal distribution and $\log_{10}(\text{count flux ratio})$ should be Gaussian distributed. Extreme X-ray variability should be a rare phenomenon and, much like extreme outliers in Gaussian distributions, can be attributed to random fluctuations in the physical mechanism that is producing the X-ray flux. If, however, there are additional physical processes that occasionally drive larger X-ray flux variations, an excess of objects should appear in the outlier tails of the $\log_{10}(\text{count flux ratio})$ distribution compared to a Gaussian distribution. Conversely, if a mechanism exists that suppresses large variations in the X-ray flux, the $\log_{10}(\text{count flux ratio})$ distribution would exhibit a large peak and smaller tails than expected from a Gaussian distribution.

Before analysing the three time-scale distributions in detail, we first determined whether the dispersion of each distribution is intrinsic or if it is largely due to measurement error. The likelihood method in Maccacaro et al. (1988) was used to deconvolve the parent distribution from the distribution of measurement errors, assuming the parent distribution is consistent with being a Gaussian. The intrinsic dispersion of the short-time-scale distribution is $\langle \sigma_p \rangle = 0.069 \pm 0.007$ which suggests, when compared to the standard deviation of the distribution ($\sigma_{\text{short}} = 0.132$), that the measurement errors provide a somewhat larger contribution to the spread of the $\log_{10}(\text{count flux ratio})$ distribution at short time-scales than the parent distribution. The intrinsic dispersions of the parent population for the intermediate and long time-scale distributions are $\langle \sigma_p \rangle = 0.172 \pm 0.014$ and $\langle \sigma_p \rangle = 0.199 \pm 0.017$, respectively. Since these values are only somewhat smaller than the standard deviation of the

⁷While we only report the results from this data set, we tested each of the samples and find similar conclusions.

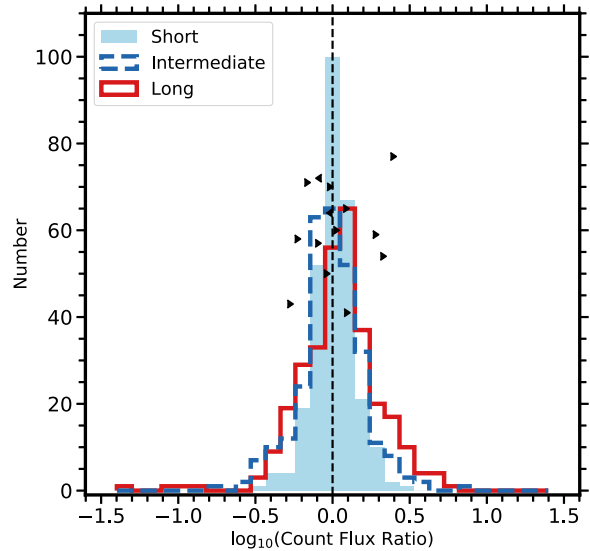


Figure 5. Distributions of count flux ratio for observations that are separated by $\Delta t \leq 0.463 \times 10^6$ s (filled light blue, 284 points), $0.463 \times 10^6 < \Delta t \leq 25.4 \times 10^6$ s (dashed blue; 297 points), and $\Delta t > 25.4 \times 10^6$ s (open red; 318 points) in the Full sample with down-sampled permutations. The vertical dashed line depicts a flux ratio of one and the black arrows show the X-ray limits and directions. An AD test of normality indicates that none of the three distributions is consistent with a Gaussian distribution. Furthermore, the three distributions are not consistent with each other according to an AD two-sample test (short-intermediate p -value = 1.6×10^{-3} ; intermediate-long p -value = 1.9×10^{-3} ; short-long p -value = 1.0×10^{-5}). A visual inspection of the three distributions suggests that the intermediate and long time-scale bins display larger count flux ratios than the short time-scale distribution which implies that extreme X-ray variations occur more frequently at larger Δt .

intermediate ($\sigma_{\text{intermediate}} = 0.207$) and long ($\sigma_{\text{long}} = 0.258$) time-scale sub-samples, the dispersion of $\log_{10}(\text{count flux ratio})$ is largely intrinsic in both distributions. Recall, however, that this analysis assumes that the parent distributions are Gaussian. If they are non-Gaussian distributions (e.g. due to additional physical mechanisms that drive extreme variations), the relationship between the intrinsic scatter and dispersion due to the measurement errors becomes more difficult to model.

We tested the consistency of each of the three distributions with a Gaussian distribution using an Anderson–Darling (AD) test of normality (Anderson & Darling 1952). We elected to use this test (as opposed to the more frequently used Kolmogorov–Smirnov test) since it is more sensitive to differences in the tails of the distributions which, in this work, are occupied by the large-amplitude variations. While this test does not account for censored data, the fraction of censored points is only ≈ 1.5 per cent and was found to have little effect on the results of the test.⁸ All three of the time-scale bins are inconsistent with a Gaussian distribution at a high confidence level (see Table 2). Within the constraints of our data, this implies that

⁸We tested the effect that the limits had on the AD normality test by drawing ten thousand random values from a uniform distribution to use as the limit values in the AD test. For upper limits on count flux ratio, the bounds of random drawing were set between the 90 per cent confidence limit value and the minimum of the full sample. For lower limits on the ratio, the bound was set between the 90 per cent confidence limit value and the maximum of the full sample. The results of the AD test with the limits included were consistent with the test without the limits.

Table 2. Results of splitting the Full sample with reduced permutations by time-scale and luminosity.

Sub-sample Name	N_{pairs}	Normality test		Symmetry test		Kurtosis		Median-based statistics	
(1)	(2)	A^2	p -value	A^2	p -value	k	σ_k^a	Median	MAD
(1)	(2)	(3)	(4)	(5)	(6)	(7)	(8)	(9)	(10)
Split by time-scale									
Short	284	2.26	9.6×10^{-6}	0.37	0.24	1.604	0.442	0.007	0.068
Intermediate	297	1.72	1.9×10^{-4}	-0.57	0.63	1.570	0.759	-0.002	0.110
Long	318	2.21	1.3×10^{-5}	-0.48	0.58	3.520	1.184	0.053	0.134
Split by L_{2500}									
Low	380	5.08	1.4×10^{-12}	-0.85	0.86	5.106	1.740	-0.001	0.102
High	278	1.58	4.7×10^{-4}	0.03	0.34	0.780	0.362	0.035	0.103

Results of the statistical tests performed on the sub-samples in Sections 4.2 and 4.3 for the Full sample with reduced epoch permutations. Columns 1 and 2 present the sub-sample name and the number of epoch pairs in that sub-sample, respectively. Column 3 reports the critical value of the AD normality test. We present the p -value of this test in column 4. Columns 5 and 6 are similar, but report the results of the AD two-sample test to determine if the distributions are symmetric. The kurtosis value and the error derived using a bootstrap re-sampling method are reported in columns 7 and 8. Columns 9 and 10 report the median and median-absolute-deviation (MAD) of the sample. While we only report the statistics from this sample, we found that the results from the other three samples yield similar conclusions.

^a The standard deviation of the distribution of kurtosis values from 5000 bootstrap re-sampling iterations.

additional physical processes are present at all time-scales making the distributions non-Gaussian.

We also tested the symmetry of each distribution by performing an AD two-sample test (Scholz & Stephens 1987) on each half of the data, split at $\log_{10}(\text{count flux ratio}) = 0$. In all three of the time-scale sub-samples, the two halves of the distributions are consistent and thus we consider them to be symmetric. The symmetry of the distributions suggests that the variability seen in our sample occurs relatively equally in both the positive and negative directions. Physical mechanisms that cause a sudden rise followed by a gradual decrease in X-ray flux (akin to what is seen in supernovae light curves) can be ruled out for the quasar population.

A visual inspection of Fig. 5 suggests that the intermediate and long time-scale distributions display an excess of large X-ray variations compared to the short time-scale distribution. An AD two-sample test was used to determine the consistency of the three distributions with each other. None of the distributions is consistent with each other according to this test (short-intermediate p -value = 1.6×10^{-3} ; intermediate-long p -value = 1.9×10^{-3} ; short-long p -value = 1.0×10^{-5}); however, the largest inconsistency occurs between the short and long time-scale distributions. Such a result may be expected since the mechanism driving this variability is able to sample a wider range of X-ray fluxes at long time-scales compared to short time-scales.

A measurement of the kurtosis of each sub-sample was also used to determine whether the amplitude of X-ray variability underpopulates the tail (e.g. a lack of large variations) or overpopulates the tail (e.g. an excess of large variations) of their respective distributions compared to a normal distribution. The kurtosis is defined as the ratio between the fourth central moment and the standard deviation to the fourth power of a distribution and largely indicates whether there is an excess of outlier data in the distribution compared to expectations for a Gaussian distribution (e.g. Livesey 2007; Westfall 2014). The kurtosis can therefore be used as a measure of the frequency at which large X-ray flux variations are produced by the underlying physical mechanisms compared to a Gaussian random fluctuation. All three distributions display a positive kurtosis (see Table 2; $k = 0$ indicates a Gaussian kurtosis) which confirms that they indeed are non-Gaussian and contain an excess of large X-ray flux variations. Extreme variations in these time-scale distributions are therefore

likely a consequence of additional physical mechanisms as opposed to the result of random fluctuations in coronal emission.

Since the three distributions of $\log_{10}(\text{count flux ratio})$ are symmetric and display an excess of kurtosis compared to a Gaussian distribution, we elected to measure the spread in the distributions using the median-absolute-deviation (MAD; Maronna, Martin & Yohai 2006), which measures the median value of the absolute deviations of each value in a distribution from the sample median. The MAD statistic is much less sensitive to the outliers of a distribution and therefore better estimates the standard deviation for non-Gaussian distributions. Furthermore, for a Gaussian distribution, MAD can be related to the standard deviation through the equation: $\sigma_{\text{MAD}} = 1.483 \times \text{MAD}$. For the short, intermediate, and long time-scale sub-samples, we find deviations of $\text{MAD} = 0.068, 0.110,$ and 0.134 , respectively. In this work, we define an ‘extreme’ variation as a $5\sigma_{\text{MAD}}$ ($7.415 \times \text{MAD}$) deviation in the distribution. Using the measured MAD values in this definition, we determine that extreme X-ray variations occur when the count flux changes by a factor of $\approx 3.19, \approx 6.54,$ and ≈ 9.85 for the short, intermediate, and long time-scales, respectively. Previous investigations have used a factor of 10 to denote an extreme X-ray variation, which we find to be a reasonable value at long time-scales. This quantification of extreme variations allows us to put some past discoveries in better context. For example, the factor of >20 variation of the luminous quasar SDSS J1539+3954 on long time-scales (Ni et al. 2020) corresponds to a $6.5\sigma_{\text{MAD}}$ event.

4.3 Extreme X-ray variability and L_{2500}

The quasar sample in this investigation spans a wide range of L_{2500} and thus can be used to investigate differences in extreme X-ray variability between quasars with bright and faint ultraviolet (UV) luminosity. To investigate the extreme X-ray variations of quasars at different luminosities, the Full quasar sample with reduced epoch permutations was split at the median luminosity ($\log_{10}(L_{2500}) = 30.4 \text{ erg s}^{-1}$) to generate two sub-samples with similar sizes. The lower luminosity quasars, however, tend to span longer rest-frame time-scales since they are preferentially detected at low redshift (see Fig. 1). Since a significant difference was found in X-ray variability between short and long time-scales in Section 4.2, an appropriate

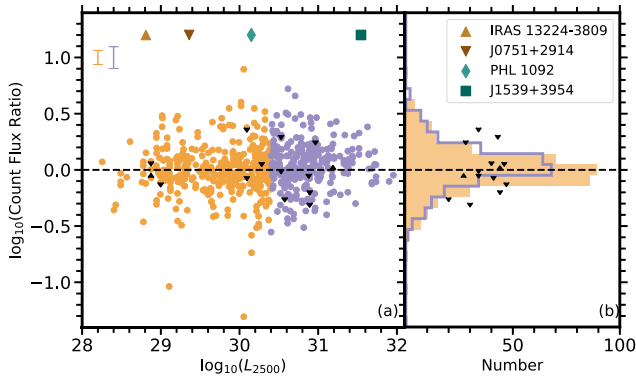


Figure 6. Panel (a): The logarithm of the count flux ratio as a function of the 2500 Å luminosity for the Full sample of quasars with down-sampled epoch permutations. The data are split by the median value of L_{2500} into bright (purple) and faint (orange) sub-samples. X-ray limits are shown by the black points, the horizontal dashed line corresponds to a count flux ratio of one and the median error bars for each sub-sample are depicted in the top left-hand corner. Also depicted are four examples of extremely X-ray variable AGNs in the literature to show with which luminosity bin they are associated (their $\log_{10}(\text{count flux ratios})$ are forced to 1.2). Panel (b): The distributions of the $\log_{10}(\text{count flux ratio})$ in the two luminosity bins. While these two distributions appear to be similar, we find that the distribution of the low-luminosity quasars is not consistent with a Gaussian with high confidence, whereas the high-luminosity quasar distribution is much more Gaussian-like (though still non-Gaussian). The low-luminosity quasar distribution is also much more tail-heavy (as determined by the kurtosis) than the high-luminosity quasars. This suggests that the low-luminosity quasars are more likely to exhibit extreme X-ray variability than would be expected from random fluctuations.

comparison of the luminosity bins can only be made when the time-scale distributions of the two luminosity sub-samples are similar. To do so, we located the upper and lower 10 per cent of time-scales in the low-luminosity sub-sample ($\Delta t > 10^{8.1}$ and $\Delta t < 10^5$ s, respectively) and removed observations with time-scales beyond those values from the low- and high-luminosity sub-samples. This approach removes the time-scale outliers in both luminosity sub-samples, and thus mitigates the biases in time-scale. An AD two-sample test reports that the Δt distributions of the two luminosity sub-samples are similar (p -value = 0.494) and thus can be appropriately compared.

Panel (a) of Fig. 6 depicts $\log_{10}(\text{count flux ratio})$ as a function of L_{2500} for both the bright (purple points; 278 measurements of 165 quasars) and faint (orange points; 380 measurements of 201 quasars) sub-samples, and the histogram of their $\log_{10}(\text{count flux ratio})$ is depicted in panel (b). As before, the intrinsic dispersion of both the low- and high-luminosity sub-samples were deconvolved from the distribution of measurement errors using the method from Maccauro et al. (1988). The standard deviation of the low-luminosity and the high-luminosity sub-sample ($\sigma_{\text{low}} = 0.218$ and $\sigma_{\text{high}} = 0.200$, respectively) is only somewhat larger than the dispersion of their parent populations ($\sigma_{\text{p, low}} = 0.177 \pm 0.015$ and $\sigma_{\text{p, high}} = 0.150 \pm 0.011$, respectively), which implies that the observed scatter is largely intrinsic.

In panel (a) of Fig. 6, we also depict the extremely X-ray variable AGN PHL 1092 (e.g. Miniutti et al. 2012), IRAS 13224–3809 (e.g. Buisson et al. 2017), SDSS J0751+2914 (Liu et al. 2019), and SDSS J1539+3954 (Ni et al. 2020), all of which have varied by more than a factor of ≈ 20 and span a wide range of L_{2500} (we force the count flux ratio to be ≈ 1.2 for each of these objects to maintain the scale of our sample). Three of these four quasars have

luminosities that overlap with the low-luminosity sub-sample defined in this investigation, while only SDSS J1539+3954 is consistent with the high-luminosity sub-sample. The luminosity distribution of these previously discovered extremely X-ray variable quasars anecdotally suggests that the lower luminosity quasars are more likely to exhibit extreme variations than the high-luminosity objects.

As before, the consistency of the luminosity distributions with a normal distribution was tested using an AD test of normality. The AD test reported that the low-luminosity sample is not consistent with a Gaussian with a high significance (p -value = 1.4×10^{-12}), whereas the high-luminosity sample is more consistent with a Gaussian distribution (p -value = 0.0047). The AD test of the high-luminosity sub-sample has a much larger p -value and thus the null hypothesis of consistency with a Gaussian cannot be rejected with high confidence. This may suggest that the mechanism driving the extreme X-ray variations in luminous, typical quasars without strong radio emission or BALs may be significantly weaker than at low-luminosities. If, however, the time-scale of this physical mechanism is dependent on physical properties of the quasar (e.g. black hole mass or luminosity), then the extreme X-ray variations in the high-luminosity quasars may be just as prevalent as in the low-luminosity sample, but may occur on an even longer time-scale than what is probed by this analysis.

A test of the similarity between the two count flux ratio distributions depicted in panel (b) of Fig. 6 was performed using the AD two-sample test. The result of this test implies that the two distributions are not similar, yet with low significance (p -value ≈ 0.004). The combination of this result and the finding that the low-luminosity sub-sample is non-Gaussian at a high confidence level whereas the high-luminosity distribution is much more consistent with a Gaussian suggests that there is likely a trend between decreasing luminosity and increasing amplitude of X-ray variability. Making additional cuts in luminosity (e.g. cutting equally into thirds) could help to further highlight differences in extreme X-ray variability at different luminosities; however, our sample is not large enough to perform such an analysis and obtain statistically significant conclusions. It would also be instructive to split each time-scale sub-sample by luminosity to investigate further this point once a larger sample can be generated.

We then examined the symmetry of the low- and high-luminosity samples using the AD two-sample test and measured their kurtosis. Both distributions are consistent with being symmetric around zero (see Table 2) and the excess kurtosis of the low-luminosity sample ($k = 5.106$) is consistent with a tail-heavy distribution, whereas the high-luminosity sample kurtosis ($k = 0.780$) is only slightly larger than what is expected for a Gaussian distribution given the uncertainty (see Table 2). This result again suggests that the low-luminosity sub-sample more frequently displays larger variations than would be expected from Gaussian random fluctuations and thus the extreme X-ray variations are likely driven by additional physical mechanisms. While the kurtosis of the high-luminosity sub-sample is positive, the value is only marginally larger than what is expected for a Gaussian distribution. An additional physical mechanism might be driving the extreme X-ray variability in this sub-sample; however, the tails of this distribution may also be driven largely by random fluctuations over the time-scales probed by this analysis. More data are needed to test further whether or not the extreme X-ray variability in high-luminosity quasars is randomly driven. We find that the spreads in the distributions of the low- and high-luminosity samples are $\text{MAD} = 0.102$ and 0.103 , respectively, which suggests that extreme $5\sigma_{\text{MAD}}$ X-ray variability occurs at count flux ratios of ≈ 5.71 and ≈ 5.80 , respectively.

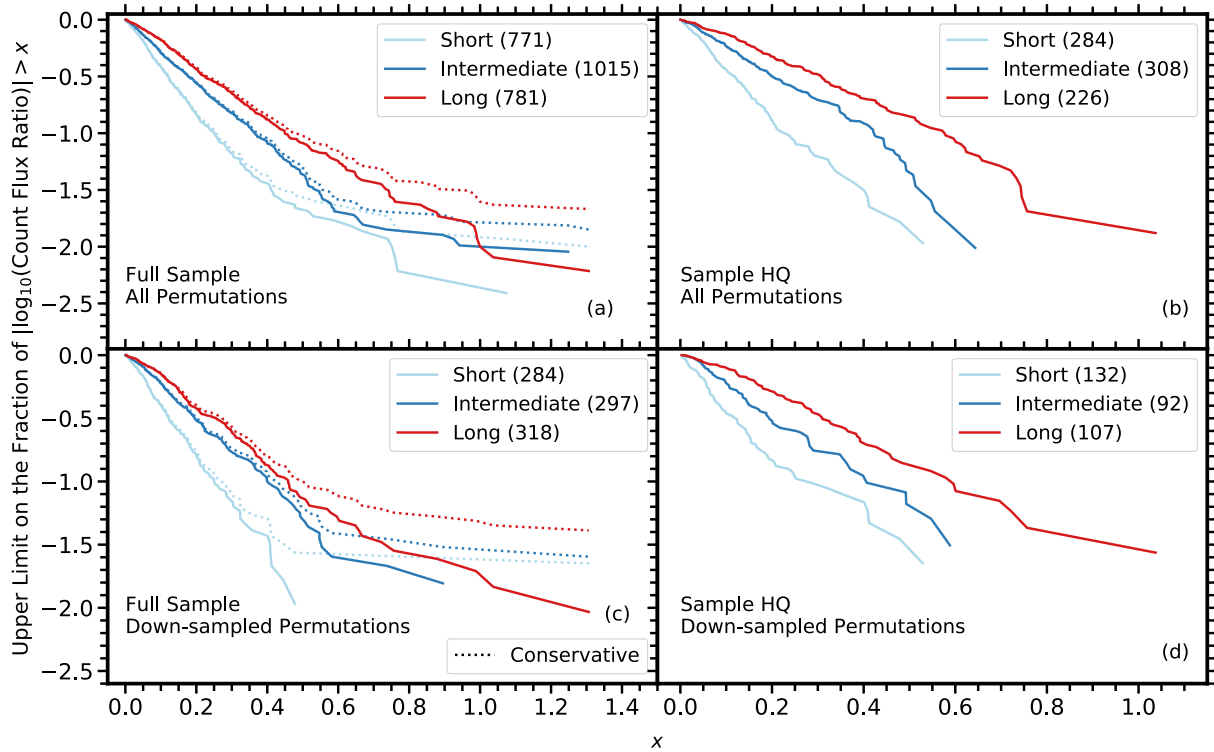


Figure 7. Each panel depicts the upper limit on the frequency at which typical quasars vary by more than a given count flux ratio, x , for the four different samples considered in this investigation. Each sample is separated into a short (cyan), intermediate (dark blue), and long (red) time-scale sub-sample as defined in Section 4.2. Panels (a) and (c) also depict the median (solid line) and conservative (dotted line) methods of treating the X-ray limits. The curves in panels (a) and (b) contain all epoch permutations of each of the quasars in their respective samples. Panels (c) and (d) depict the down-sampled counterparts of the previous two panels and thus are not as heavily weighted toward quasars with many observations. Each of the four panels indicates that the rate of observed extreme intrinsic variation increases with increasing time-scale.

4.4 Frequency of extreme X-ray variability

A primary purpose of this investigation is to quantify the frequency of intrinsic extreme variations in X-ray flux for typical quasars to understand better the nature of the X-ray coronal region and innermost accretion flow. To estimate the frequency of extreme X-ray variation, we adopted the statistical method from Section 3.3.3 of Gibson & Brandt (2012). This technique employs binomial statistics to estimate the probability that the magnitude of $\log_{10}(\text{count flux ratio})$ in a quasar is greater than a given value, $|x|$. If N is the number of measurements in our sample that satisfy this condition, then the probability that a quasar has $\log_{10}(\text{count flux ratio}) > |x|$ can be computed by solving the binomial equation assuming that there is a 95 per cent binomial probability of finding $N + 1$ such objects. The frequencies calculated in this investigation include the intrinsic variations of the quasars as well as the variations due to the measurement errors, which are difficult to model, and thus the frequency of extreme X-ray variability should be considered as upper limits. Insofar as the variations in the measurement uncertainties are small, the upper limits on the fraction of extreme X-ray variability found in this Section can be representative of the true fraction; however, we will conservatively report them as upper limits. Moreover, the estimated frequencies presented in this Section are only applicable to quasars that share the same characteristics as our quasar sample (e.g. non-BAL, radio-quiet quasars).

Ideally, this analysis would be performed entirely with well-measured count flux ratios; however, there were a few objects in this work that were not detected in X-rays and thus the 90 per cent confidence limits on the count flux ratio are reported. We incorporated

these limits into the calculation of the frequency in two different ways. First, we conservatively assume that all of the limits maximally vary and are given a value equal to the maximum count flux ratio found among the full population. This method assumes that all of the limits are extremely X-ray variable; however, this is a conservative approach because, in some cases, even a slight decrease in the X-ray flux of a quasar could cause the quasar to be fainter than the limiting flux threshold of a *Chandra* observation and thus, it can no longer be well detected. A likely more realistic method of incorporating the X-ray limits (hereafter, the median method) is to evaluate the $\log_{10}(\text{count flux ratio})$ of the limits with respect to the ratios of objects with similar Δt values in Fig. 4. For each of the limits depicted in Fig. 4, we compare the count flux ratio (using the 90 per cent confidence limit as the ‘true’ count value) with nearby count flux ratio measurements (i.e. Δt is within a factor of 3). If the count flux ratio of the limit is consistent within 1σ of its neighbors, we consider the limit to vary as the median of the neighboring objects. If the count flux ratio of the limit exceeds the 1σ range, we assume maximal X-ray variability as in the conservative method. While this method may not be precise, we find it unlikely that *all* of the X-ray non-detections have varied extremely, particularly considering the numerical distribution of limit values in Fig. 4. We report the results of both methods in the following discussion.

We first investigated the upper limit on the frequency of X-ray variation for the quasars in our samples split by time-scale from Section 4.2. Fig. 7 depicts the results of the binomial analysis on all four of the samples generated in this work. Panels (a) and (b) include all of the epoch permutations for each quasar for the Full

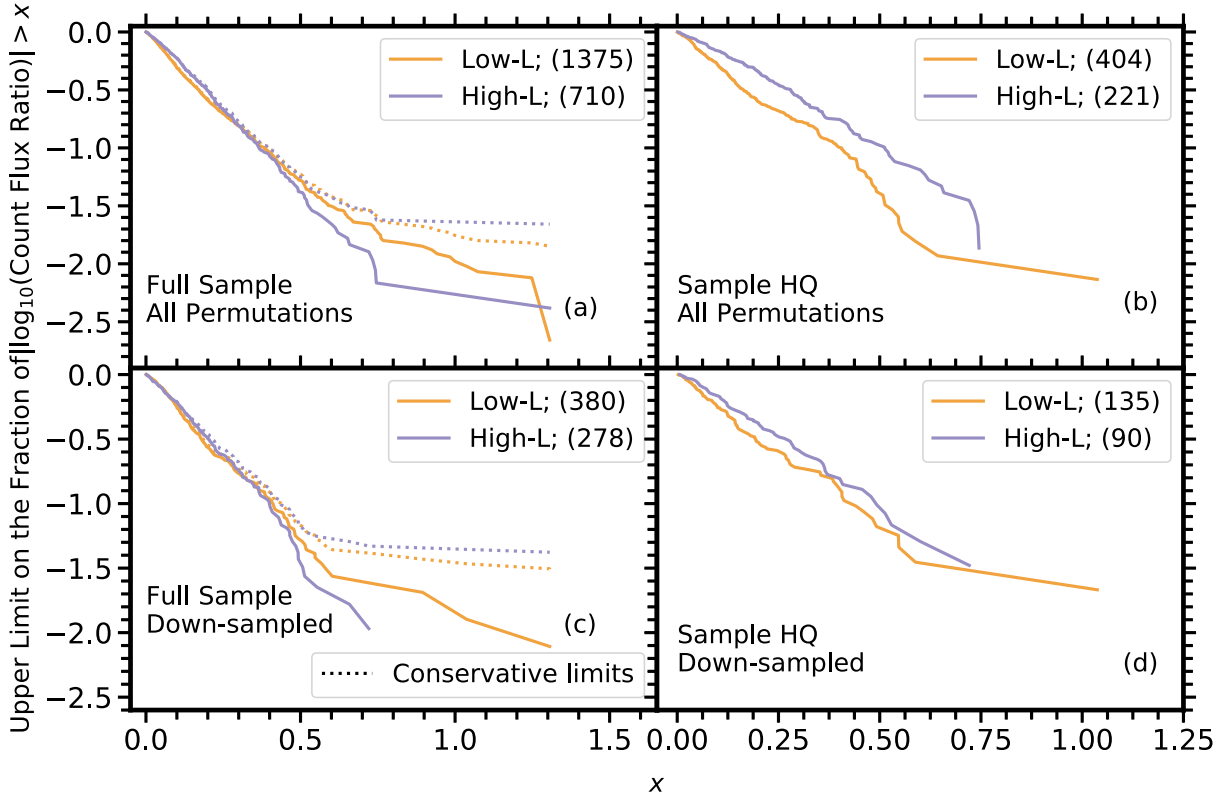


Figure 8. Similar to Fig. 7, however instead of splitting by time-scale, the samples were split at the median luminosity into high-luminosity (purple) and low-luminosity (orange) sub-samples (see Section 4.3). The upper limits on the frequency in these two sub-samples are much more consistent than when splitting by time-scale; however, at large-amplitude variations, the frequency of X-ray variability in the low-luminosity sub-sample is generally larger than that of the high-luminosity sub-sample on similar time-scales. The sudden decrease in the frequency at large count flux ratio in the low-luminosity sub-sample depicted in panel (a) is the result of removing some of the extreme variations at long time-scales when matching the low- and high-luminosity sub-samples in time-scale.

sample and Sample HQ, respectively. In panel (a), we also depict the two methods of incorporating the X-ray non-detections into the calculation (solid line, median method; dotted line, conservative method). For clarity, we report the logarithm of the frequency for each given sub-sample. For example, panel (a) of Fig. 7 reports that an X-ray variation by a factor of 10 occurs for $< 10^{-1.6} \approx 2.5$ per cent of observations at long time-scales using the conservative limit approach and $< 10^{-2.0} \approx 1.0$ per cent of observations using the median limit approach. From panel (b), which contains no X-ray limits, the same amplitude of variation occurs in $< 10^{-1.85} \approx 1.6$ per cent of observations at long time-scales. A comparable estimate of the frequency for this factor of 10 variation is ≈ 4.0 per cent using the estimates in Gibson & Brandt (2012), and thus our sample provides significantly improved constraints on extreme X-ray variability.

Depicted in panels (c) and (d) of Fig. 7 are the results of the analysis when performed on the down-sampled versions of the Full sample and Sample HQ, respectively. In Section 4.2, we have defined ‘extreme’ variations as the $5\sigma_{\text{MAD}}$ deviation from the median for each of the three time-scale sub-samples of the Full sample with reduced permutations. From panel (c) of Fig. 7, the upper limit on the frequency of these extreme variations is between < 1.0 – < 3.1 , < 1.9 – < 3.3 , and < 1.9 – < 4.7 per cent at short, intermediate, and long time-scales (where we report the median–conservative method of incorporating the limits).⁹ Panel (d), which is not affected by

X-ray limits, reports a frequency between the median and conservative approaches in panel (c) for the long time-scale sub-sample (< 3.2 per cent); however, the short and intermediate time-scale sub-samples do not extend to the 5σ value computed in Section 4.3 and thus no precise limit can be determined beyond what is found in panel (c). All of the panels in Fig. 7 demonstrate that extreme intrinsic X-ray variability occurs more frequently at long time-scales than at short time-scales and that it is a very rare phenomenon. Although the frequencies of extreme X-ray variability derived above are small, we do not consider them to be consistent with zero since the kurtosis values of the three time-scale distributions, which can also be used as a measure of the frequency of extreme variations, are not consistent with zero (see Section 4.2). Radio-quiet, non-BAL quasars that are found to exhibit such extreme X-ray variability should therefore be closely monitored to understand better the driving mechanisms of this quantifiably remarkable phenomenon.

The frequency of extreme X-ray variation in the two luminosity sub-samples presented in Section 4.3 was also calculated. Fig. 8 depicts the four samples of quasars in the same manner as in Fig. 7. In all of the panels, the upper limit on the frequency of variation in the low- and high-luminosity sub-samples is very similar for small-amplitude X-ray variations, but as the amplitude increases the frequency of occurrence for the low-luminosity quasars tends to be larger than that of the high-luminosity quasars when the upper limits are incorporated using the median method.¹⁰ From panel (c)

⁹The short and intermediate time-scale bins do not extend to the 5σ value when treating the limits using the median method, so we instead report the smallest value of the frequency for these sub-samples.

¹⁰This is apparently not the case in panel (b); however, we found that a single object with numerous observations is causing the large difference between

of Fig. 8, the extreme variations defined in Section 4.3 in the high- and low-luminosity sub-samples occur at a rate of < 1.0 – < 4.9 and < 2.4 – < 4.0 per cent, respectively, where the median-conservative limit approaches are reported as before. Once again, these curves were derived from the luminosity sub-samples that were designed to have similar time-scale distributions. If the physical driver of extreme variations is luminosity-dependent, then the high-luminosity quasars might vary extremely ($\gtrsim 10$ times) at a similar frequency as the low-luminosity quasars, but on a time-scale even longer than that probed by this analysis. Splitting the luminosity bins by the median time-scale ($\Delta t = 6.76 \times 10^6$ s), we find that the low-luminosity, long time-scale sub-sample has the largest frequency of extreme X-ray variability (< 3.0 per cent using the median method); however, additional data are required to increase the sizes of the samples to confirm this result.

Figs 7 and 8 both demonstrate that extreme X-ray variability occurs very infrequently in the sample that was constructed in this work. The low rate of occurrence of these events likely indicates that extremely X-ray variable quasars are rare objects in the overall majority radio-quiet quasar population. Another possibility, at least in principle, is that the duty cycle of extreme X-ray variability is low and the X-ray light curves are not sampled sufficiently densely to capture these events when they occur. Our investigation, however, was designed to include a large sample of X-ray observations of quasars that span a wide range of rest-frame time-scales (up to ≈ 12 yr) in order to detect extreme X-ray variability even in the case of a small duty cycle. Unless the duty cycle is very small, it is likely that the low frequencies computed in this Section reflect the fact that extremely X-ray variable quasars are rare objects in the overall quasar population.

In Section 5, we report some X-ray and optical/UV emission-line properties of three SDSS quasars that we discovered in our work to have exhibited extreme X-ray variability according to the condition derived in Section 4.4 for long time-scales (a flux ratio > 9.85). Each of these quasars was found to have notably hard X-ray spectra in at least one epoch which generally indicates that the X-ray spectrum is absorbed (though, the quasar J1420+5254 may also show evidence of intrinsic extreme X-ray variability; see Section 5.3). X-ray absorption in quasars can be complex (e.g. Gallagher et al. 2002, 2006) and can come from many different physical sources. For example, such absorption could possibly be attributed to a BAL wind (and any associated shielding gas) since blue, type 1 quasars with heavy X-ray absorption are typically found to possess BALs (e.g. Brandt, Laor & Wills 2000). If this is the case, the extreme X-ray variability for these quasars might be the result of a larger scale environment change and not an intrinsic change in the corona and innermost accretion flow, and thus following Section 1 these quasars should be removed from our analysis. Alternatively, the absorption in these quasars could potentially be due to shielding by a thick inner accretion disc. At large viewing angles, the central X-ray corona may be absorbed by the thick disc, but changes in the covering factor of the corona by the disc due to variations in the size of the corona or azimuthal asymmetries of the inner disc (e.g. Liu et al. 2019; Ni et al. 2020) may cause an extreme X-ray variability event. In this case, the extreme variations of these quasars would be due to changes in the innermost accretion flow, and thus we should retain these quasars in our analysis.

We cannot directly confirm either scenario for our three newly discovered extremely X-ray variable quasars without follow-up

the two samples. Removing the permutations in panel (d) reduces the effect of this issue.

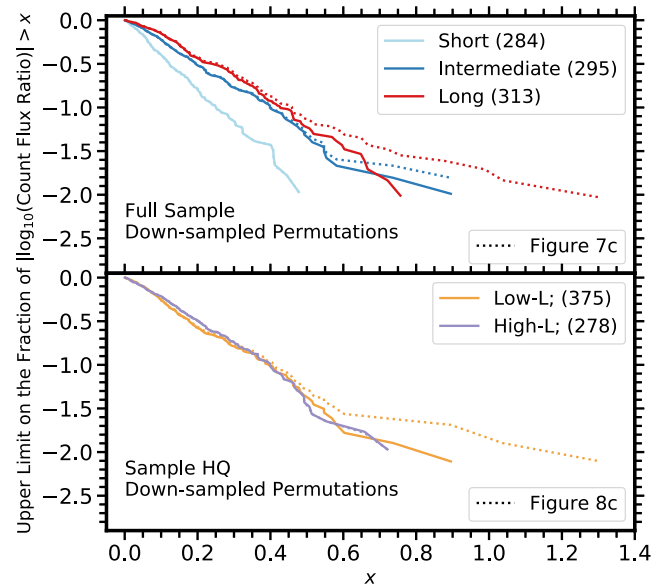


Figure 9. The frequencies of X-ray variability in the three time-scale bins from Section 4.2 (top panel) and two luminosity bins from Section 4.3 (bottom panel) after removing the three quasars that we conservatively assume to extremely vary due to X-ray absorption by a BAL wind (see Section 5). The solid curves depict the frequencies after removing these quasars and the dotted curves depict the results presented in panel (c) of Fig. 7 for the time-scale sub-samples (top panel) and Fig. 8 for the luminosity sub-samples (bottom panel). X-ray limits are treated using the median method for each curve. After removing these potentially X-ray absorbed quasars, we find that the frequency of extreme X-ray variability marginally decreases in the low-luminosity, intermediate-time-scale, and long-time-scale sub-samples. The frequencies depicted in both panels are only mildly smaller than those in Figs 7 and 8 which illustrates the robustness of the results of our full analysis and further demonstrates that extreme X-ray variability in radio-quiet, non-BAL quasars is a rare phenomenon.

spectroscopic observations of their rest-frame UV emission (note these quasars lie at $z < 1.7$, so the SDSS spectra do not cover the CIV region). We therefore conservatively assume in this paragraph that all three quasars that may be X-ray absorbed in at least one epoch are BAL quasars and thus they should be removed from the sample following Section 3.2. Fig. 9 depicts the frequency of extreme X-ray variability after removing these objects. The top panel of Fig. 9 depicts the three time-scale bins in the reduced epoch permutation sample akin to panel (c) of Fig. 7, and the bottom panel similarly presents the two luminosity bins as shown in panel (c) of Fig. 8. In both panels, we treat the X-ray limits using the median method. Fig. 9 clearly illustrates that the frequencies of the intermediate-time-scale, long-time-scale and the low-luminosity bin decrease somewhat compared to those in Figs 7 and 8, respectively, whereas the frequencies computed for the short-time-scale and high-luminosity sub-samples are not affected by the removal of these quasars. The mild decrease illustrates the robustness of the results in Figs 7 and 8 and further confirms that intrinsic extreme X-ray variability is a rare phenomenon.

Although the frequency of intrinsic extreme X-ray variations is very low, our analysis indicates that they are not likely an artefact of statistical fluctuations, rather seeming to be driven by at least one additional physical mechanism. Models of the corona and innermost accretion flow must therefore reproduce the rarity of these extreme X-ray variability events without considering them to be merely random fluctuations of the X-ray flux.

5 EXTREMELY X-RAY VARIABLE OBJECTS

During the course of this investigation, we discovered three quasars that have varied extremely (by $\gtrsim 9.85$ times) in their full-band count flux consistent with the threshold derived in Section 4.4. These three quasars were used in the analyses reported in Section 4.4 (aside from Fig. 9, where they were explicitly removed). All three of these quasars have 2500 Å luminosity (derived from the single-epoch *i*-band magnitude in the SDSS DR14Q catalogue) consistent with our low-luminosity bin. Here, we present a brief overview of the basic properties of these three objects. More detailed investigations into the relationship between the UV/optical and X-ray light curves of these objects will be reserved for future work.

5.1 SDSS J141531.93+112850.7

There were only two observations of SDSS J1415+1128 ($z = 0.360$; $\log_{10}(L_{2500}) = 29.11 \text{ erg s}^{-1}$) in the *Chandra* archive that satisfied our requirements, with the first taken in 2000 April (≈ 18 ks exposure) and the second in 2005 March (≈ 84 ks exposure). A third observation was found from 2013 April; however, the quasar coincided with an ACIS chip-gap and thus the observation was automatically removed from our analysis. Between 2000 and 2005 ($\Delta t \approx 1.15 \times 10^8$ s; ≈ 1330 d), this object increased in full-band count flux by a factor of ≈ 11 . The measurement from the observation in 2013 suggests that the flux then decreased by a factor of ≈ 2.7 ; however, a more detailed analysis is required since in 2013 the quasar lies on a chip gap and thus the measurement is likely highly uncertain.

Provided that the UV luminosity does not change significantly over time, the expected X-ray-to-optical spectral slope is $\alpha_{\text{ox}} = -1.37$, using the relationship between $\log_{10}(L_{2500})$ and α_{ox} from Just et al. (2007).¹¹ The measured values from the 2 keV flux density are $\alpha_{\text{ox}} = -1.87$ and -1.46 for the first and second epoch, respectively. Comparing the measured values of α_{ox} with the expected value indicates that the X-ray emission from the quasar was significantly weaker than expected in the first epoch ($\Delta\alpha_{\text{ox}} = -0.50$) but consistent with being X-ray normal in the second epoch ($\Delta\alpha_{\text{ox}} = -0.09$) considering the intrinsic dispersion of α_{ox} values in Table 5 of Steffen et al. (2006). Using the hard-to-soft band ratios and the *Chandra* PIMMS (Portable, Interactive MultiMission Simulator)¹² software, we measured the effective power-law photon index, Γ , for the faint and bright epochs (assuming only Galactic absorption). The first, fainter epoch has a flat effective photon index ($\Gamma = 1.0_{-0.5}^{+0.5}$), albeit with a large uncertainty, whereas the second, bright epoch has a steeper effective photon index ($\Gamma = 1.85_{-0.10}^{+0.09}$) akin to that of a typical quasar ($\Gamma = 1.8$; e.g. Scott et al. 2011). The hard spectrum in the first epoch suggests the presence of X-ray absorption which may indicate that a BAL wind is present in this quasar that we are unable to observe with SDSS. The quasar gets brighter and softer in the second epoch as expected if a simple X-ray absorber moves out of the line of sight to the X-ray continuum. If a BAL wind is present, the extreme X-ray variability would be the result of a larger scale environment change and not an intrinsic change in the corona and innermost accretion flow; therefore, we remove this quasar when performing the statistical analysis presented in Fig. 9.

The $H\beta$ emission-line width in this blue, type 1 quasar is not narrow ($\text{FWHM} \approx 6000 \text{ km s}^{-1}$) and the [O III] 5007 Å emission-line strength is consistent with that of a typical quasar ($\text{EW} \approx 19$ Å)

¹¹ $\alpha_{\text{ox}} = 0.3838 \times \log_{10}(f_{2 \text{ keV}}/f_{2500})$, where $f_{2 \text{ keV}}$ and f_{2500} are the flux densities at 2 keV and 2500 Å, respectively.

¹²<https://cxc.harvard.edu/toolkit/pimms.jsp>

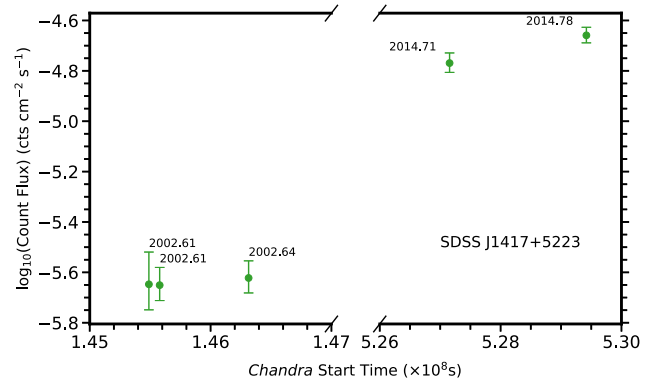


Figure 10. The full-band count flux as a function of the *Chandra* start time for the five observation epochs of SDSS J1417+5223. The values above the data points report the decimal year of the *Chandra* observation. The maximum count flux increased by a factor of ≈ 9.8 over ≈ 3472 rest-frame days for this quasar.

according to our fits to the SDSS spectrum. This object is also reported in the 2XMM serendipitous source catalogue (Watson et al. 2009) from *XMM-Newton* observations in 2001 and 2002, which are between the *Chandra* observations. Both *XMM-Newton* observations confirm that the source continued getting brighter between the *Chandra* measurements. New observations of this object are required to determine if the flux has continued to increase or if the flux peak occurred in 2005.

5.2 SDSS J141751.13+522311.0

There are five serendipitous *Chandra* observations of SDSS J1417+5223 ($z = 0.281$; $\log_{10}(L_{2500}) = 28.76 \text{ erg s}^{-1}$) with three in 2002 August/September (≈ 122 ks of stacked exposure time) and two more in 2014 September/October (≈ 34 ks of stacked exposure time) as depicted in Fig. 10. The X-ray flux of this quasar has increased between these two epochs ($\Delta t \approx 3.0 \times 10^8$ s; ≈ 3472 d) by a factor of ≈ 9.9 . From the single-epoch UV luminosity and the relationship in Just et al. (2007), the expected X-ray-to-optical spectral slope is $\alpha_{\text{ox}} = -1.32$ for this quasar. In 2002, this quasar was X-ray weaker than expected, with a minimum $\alpha_{\text{ox}} = -1.80$ ($\Delta\alpha_{\text{ox}} = -0.48$); however, in 2014 the X-ray flux significantly increased, corresponding to a value of $\alpha_{\text{ox}} = -1.43$ ($\Delta\alpha_{\text{ox}} = -0.09$), which indicates that this quasar became X-ray normal. We measured the effective photon indices using the stacked observations in 2002 and 2014, respectively, since there is only a small temporal separation between the measurements in these two epochs. We find a similar effective photon index between 2002 ($\Gamma = 1.23_{-0.20}^{+0.17}$) and 2014 ($\Gamma = 1.13_{-0.09}^{+0.09}$). The consistently hard spectrum again suggests that the X-rays are being absorbed in both epochs, though it is puzzling that the source has retained a hard X-ray spectrum when its flux returns to a nominal level for a typical quasar. As before, if a BAL wind is the primary reason for the absorption, this quasar must be removed from the analysis in Section 4.4, which we do when performing the statistical analysis for Fig. 9.

Our fit of the SDSS spectrum again indicates that this quasar has a broad $H\beta$ emission line ($\text{FWHM} \approx 15000 \text{ km s}^{-1}$) and it exhibits similar [O III] 5007 Å emission strength compared with that of a typical quasar ($\text{EW} \approx 11$ Å). This object is also reported in the 3XMM serendipitous catalogue (Rosen et al. 2016) and was included in the the AGN X-ray variability work of Vagnetti et al. (2016). The time-scale between the *XMM-Newton* observations from 2000 July

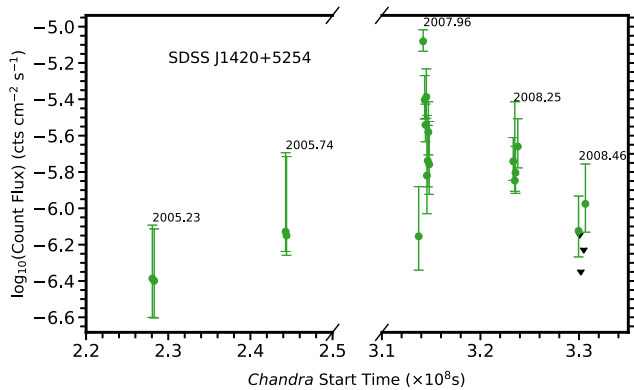


Figure 11. The full-band count flux as a function of the *Chandra* start time for the 22 observation epochs of SDSS J1420+5254. The values above the data points report the approximate decimal year of the serendipitous *Chandra* observations. The count flux increased maximally by a factor of ≈ 21 over ≈ 439 rest-frame days for this quasar.

that were used in that investigation is only ≈ 1.3 d and no noticeable difference in the X-ray flux was reported. The full-band flux value in the *XMM-Newton* observation in 2000, however, is ≈ 3 times fainter than the 2002 *Chandra* observation which suggests that this quasar has increased in flux by a total factor of ≈ 29 from 2000 to 2014. One additional *XMM-Newton* observation is reported in the 3XMM catalogue that was not included in the Vagnetti et al. (2016) investigation from 2014 which has a full-band X-ray flux value consistent with the 2014 *Chandra* observation. The three *Chandra* observations in 2002 and the two in 2014 also suggest that this quasar does not vary significantly on short time-scales and thus this appears to be the first reported instance of extreme X-ray variability from this quasar.

5.3 SDSS J142037.84+525452.8

SDSS J1420+5254 ($z = 1.269$; $\log_{10}(L_{2500}) = 30.05$ erg s $^{-1}$) was observed 22 times with *Chandra* as part of the AEGIS-X survey (e.g. Laird et al. 2009), which was a deep observation of the Extended Groth Strip between 2005 and 2008. The full-band X-ray light curve for this object is depicted in Fig. 11, where the full-band count flux values of the X-ray detections (upper limits) are depicted by the green circular points (black downward arrows). We found that the largest factor by which the full-band count flux of this object varied was ≈ 21 on a time-scale of $\Delta t \approx 3.8 \times 10^7$ s (439 d) in the rest frame. This object also exhibited short-time-scale extreme variability by a factor of ≈ 12 on a time-scale of $\Delta t \approx 2.0 \times 10^5$ s (2.73 d) in the rest frame. This quasar was not detected by *Chandra* in three observations; therefore, the X-ray flux might have decreased by an even larger factor (see Fig. 11).

Generally, the number of full-band counts in each epoch is low, which yields multiple instances in which this quasar is not detected in either the soft or the hard band, but is detected in the full band, making it difficult to estimate the shape of the X-ray spectrum. For example, the epoch with the lowest count flux value, which occurred in 2005 March, did not have sufficient counts in the soft band to be detected, but was detected in the hard and full bands. We derived a limit on the effective photon index to be $\Gamma < 0.5$ and, using the full-band counts, we found that $\alpha_{\text{ox}} = -1.90$ in this epoch, which suggests that it is X-ray weak compared to the expectation ($\alpha_{\text{ox}} = -1.50$). In the bright state (2007 December), we found that $\alpha_{\text{ox}} = -1.34$ ($\Delta\alpha_{\text{ox}} = 0.16$) and we found a steep effective photon index

($\Gamma = 2.5^{+0.4}_{-0.5}$) consistent with that of a typical quasar. As before, the transition from the flat, X-ray weak state to the steep, X-ray brighter state may suggest that this quasar is absorbed.

Since this quasar was observed over many more epochs than the previous objects, we further investigated the X-ray variability of this quasar by limiting our consideration to the epochs in which the quasar was detected in all three bands (seven epochs). After limiting to only these epochs, the quasar still exhibits extreme X-ray variability, dropping from the aforementioned high state by factor of ≈ 14 on a time-scale of $\Delta t \approx 7.1 \times 10^6$ s (82 d) in the rest frame. We found that $\alpha_{\text{ox}} = -1.78$ in this well-detected low state (2008 June) and that the effective photon index remained steep ($\Gamma = 1.9^{+0.9}_{-1.1}$) as in the bright state. Unlike before, this extreme decrease in X-ray flux but similarly steep effective photon index may suggest that this variability may be intrinsic to the coronal region and innermost accretion flow. It therefore seems possible that the extreme X-ray variations are caused by either absorption, intrinsic fluctuations, or a combination of the two. Neither the rest-frame optical nor the C IV emission-line region are present in the SDSS spectrum; thus, we cannot determine if this quasar exhibits similar emission-line properties to the other extremely X-ray variable quasars (e.g. Liu et al. 2019), nor can we definitively determine if there is a BAL present in the spectrum. Although, there may be evidence of intrinsic X-ray variability, this quasar exhibited a flat X-ray spectrum in at least one epoch; therefore, we conservatively assumed that the variations were caused by BAL absorption and thus removed this object in Fig. 9. Additional spectral observations of both the rest-frame optical and the C IV emission-line region are required to understand better the nature of the X-ray variability of this object.

6 SUMMARY AND FUTURE WORK

In this investigation, we compiled a large sample of quasars that had multiple, serendipitous *Chandra* observations in order to constrain the frequency of extreme X-ray variability intrinsic to the corona and innermost accretion flow among typical quasars. Radio-loud and BAL quasars were removed from the sample since variations of their X-ray flux can arise from larger scale environmental effects (e.g. a jet contribution or wind-associated absorption). We generated a Full sample of 1598 sensitive observations of 462 quasars, along with a high-quality sample of 583 observations of 185 quasars, in which all observations resulted in an X-ray detection. The light curves of frequently observed quasars in these data sets were also down-sampled to reduce the weight of any one quasar with many observations in the sample. The Full sample of quasars with reduced epoch permutations was split into three time-scale bins (short, intermediate, and long) and two luminosity bins (faint and bright) to investigate the frequency of extreme X-ray variations as a function of these properties. The main results of this analysis are the following:

(i) All three time-scale bins were not consistent with a Gaussian distribution according to an AD test of normality, which suggests that the extreme X-ray variations are not a result of random fluctuations in the coronal emission. Rather, it is likely that an additional physical mechanism acting occasionally drives this extreme variability. Additionally, the long time-scale bin was found to exhibit larger amplitude X-ray variations more frequently than the short or intermediate time-scale bins compared to what would be produced by random fluctuations (Section 4.2).

(ii) We used the median-absolute-deviation to define ‘extreme’ $5\sigma_{\text{MAD}}$ variations in our three time-scale sub-samples. Our analysis indicates that extreme X-ray variations occur when the flux changes

by a factor of ≈ 3.19 , ≈ 6.54 , and ≈ 9.85 at short ($\Delta t \lesssim 5.3$ d), intermediate ($5.3 \lesssim \Delta t \lesssim 294$ d), and long ($\Delta t \gtrsim 294$ d) time-scales, respectively (Section 4.2). At long time-scales, we confirm that the factor of ten used in the literature to define extreme X-ray variations is a reasonable choice for the majority population of quasars.

(iii) The distribution of $\log_{10}(\text{count flux ratio})$ in the low-luminosity sub-sample is not consistent with a Gaussian at a high confidence level, whereas the high-luminosity sub-sample is much more consistent with a Gaussian according to an AD normality test. This again suggests that the extreme X-ray variations in low-luminosity quasars arise from an additional physical mechanism whereas the high-luminosity sample is either more consistent with random fluctuations, or the physical mechanism operates on longer time-scales than at lower-luminosity (Section 4.3). The extreme $5\sigma_{\text{MAD}}$ X-ray variations occur when the count flux ratio is ≈ 5.71 and ≈ 5.80 in the low-luminosity and high-luminosity sub-samples, respectively.

(iv) Using binomial statistics, we estimated the frequency of extreme X-ray variations for the three time-scale bins (Fig. 7) and the two luminosity bins (Fig. 8). The frequency of extreme X-ray variations clearly increases with time-scale, and it appears to be larger in low-luminosity quasars (Section 4.4).

(v) The results of the binomial analysis indicate that the frequency of extreme X-ray variations in the short, intermediate, and long time-scale bins are < 1.0 , < 1.9 , and < 1.9 per cent, respectively, using the definition of extreme variability at the $5\sigma_{\text{MAD}}$ deviation and using the median method of treating the X-ray limits. Furthermore, extreme X-ray variations in the low-luminosity and high-luminosity sub-samples occur in < 2.4 and < 1.0 per cent of observations (Section 4.4). Extreme X-ray variability that is intrinsic to the coronal region is, thus, a rare phenomenon.

(vi) Finally, we found three quasars that have exhibited extreme X-ray variations on long time-scales. All three of the quasars have luminosities consistent with our low-luminosity bin and have varied by more than a factor of 9.85. These quasars might be X-ray absorbed in at least one epoch (see Section 5) and that absorption may be from an undetectable BAL wind. Conservatively assuming that these three are BAL quasars, we re-computed the frequencies of extreme X-ray variability. Fig. 9 depicts that the frequencies of extreme X-ray variability after removing the three potential BAL quasars marginally decreases, further confirming the rarity of these extreme events and the robustness of our statistical conclusions. Additional observations of these objects are needed to probe better their variability properties.

This work could be extended in a few different ways. One way to increase the sample size would be to relax the *i*-band magnitude constraint imposed; however, doing so would significantly increase the number of X-ray count limits in the sample and thus more advanced statistical analyses would be required. Such analyses could not be performed in this work since our sample contained upper and lower limits. Future investigations will have to create a new metric for measuring the variability amplitude such that the limits point in a uniform direction; however, careful consideration must be made to ensure that the new measurement does not introduce biases. Another extension of this work that can be done in the near future will be to incorporate data from the eight epochs of the *eROSITA* all-sky survey (Merloni et al. 2012), which will greatly enhance the sample size of bright quasars that can be used to increase the statistical power of the results. A brighter *i*-band magnitude limit will need to be imposed since the median flux of the quasars in our investigation is ≈ 3 times fainter than the projected limiting flux values of a single *eROSITA* epoch; however, the large area of the survey should add many more quasars to the sample. The additional data will be particularly useful

for understanding better the difference in the frequency of extreme X-ray variability between the low-luminosity and high-luminosity quasars.

Another follow-up investigation would be to compare the X-ray variability properties, including the frequency at which extreme X-ray variability occurs, of radio-loud and BAL quasars to our sample of typical radio-quiet quasars. A recent X-ray investigation of radio-loud quasars has suggested that the X-ray emission in some populations of radio-loud quasars still largely originates in the corona instead of being enhanced by the jet, as has been generally accepted (Zhu et al. 2020). Comparing the X-ray variability properties, including the rates of extreme X-ray variability, of radio-loud quasars and our typical radio-quiet quasars, could provide further insights into the origin and behaviour of the X-ray emission in these radio-loud quasars.

Additionally, a more detailed investigation of the three extremely X-ray variable quasars discussed in Section 5 would aid our understanding of the physical nature of these extreme objects. A joint investigation of the extreme X-ray variability along with the variability (or lack thereof) at other wavelengths could provide further insight into the connections between the X-ray and optical/UV emission in quasars (e.g. Liu et al. 2019; Ni et al. 2020). Since none of these quasars were observed recently in X-rays, obtaining new *Chandra* (or other X-ray) observations of these quasars would also be useful to determine how their X-ray fluxes have changed since their final observations. Obtaining rest-frame UV spectra would also allow us to determine if they are BAL quasars and measure their C IV emission lines.

ACKNOWLEDGEMENTS

We thank the referee for a constructive and prompt report. JD, WNB, SZ, and QN acknowledge support from NASA ADP grant 80NSSC18K0878, *Chandra* X-ray Center grant G08-19076X, the V. M. Willaman Endowment, and Penn State ACIS Instrument Team Contract SV4-74018 (issued by the *Chandra* X-ray Center, which is operated by the Smithsonian Astrophysical Observatory for and on behalf of NASA under contract NAS8-03060). BL acknowledges financial support from NSFC grants 11991053 and 11673010 and National Key Research and Development Program of China grant 2016YFA0400702. The *Chandra* ACIS team Guaranteed Time Observations (GTO) utilized were selected by the ACIS Instrument Principal Investigator, Gordon P. Garmire, currently of the Huntingdon Institute for X-ray Astronomy, LLC, which is under contract to the Smithsonian Astrophysical Observatory via Contract SV2-82024.

For this research, we have used the PYTHON language along with ASTROPY¹³ (Price-Whelan et al. 2018), SCIPY¹⁴ (Virtanen et al. 2020), and TOPCAT¹⁵ (Taylor 2005).

DATA AVAILABILITY

The data used in this investigation are available in the article and in its online supplementary material. See Appendix A for more details.

REFERENCES

- Anderson T. W., Darling D. A., 1952, *Ann. Math. Stat.*, 23, 193
Becker R. H., White R. L., Helfand D. J., 1995, *ApJ*, 450, 559

¹³<https://www.astropy.org/>

¹⁴<https://www.scipy.org/>

¹⁵<http://www.star.bris.ac.uk/~mbt/topcat/>

- Brandt W. N., Laor A., Wills B. J., 2000, *ApJ*, 528, 637
- Broos P. S., Feigelson E. D., Townsley L. K., Getman K. V., Wang J., Garmire G. P., Jiang Z., Tsuboi Y., 2007, *ApJS*, 169, 353
- Buisson D. J. K., Lohfink A. M., Alston W. N., Fabian A. C., 2017, *MNRAS*, 464, 3194
- Carnerero M. I. et al., 2017, *MNRAS*, 472, 3789
- Condon J. J., Cotton W. D., Greisen E. W., Yin Q. F., Perley R. A., Taylor G. B., Broderick J. J., 1998, *AJ*, 115, 1693
- Croom S. M., Smith R. J., Boyle B. J., Shanks T., Miller L., Outram P. J., Loaring N. S., 2004, *MNRAS*, 349, 1397
- Croom S. M. et al., 2009, *MNRAS*, 392, 19
- Davis J. E. et al., 2012, Proc. SPIE Conf. Ser. Vol. 8443, Raytracing with MARX: X-ray Observatory Design, Calibration, and Support. SPIE, Bellingham, p. 84431A
- Dawson K. S. et al., 2016, *AJ*, 151, 44
- Eisenstein D. J. et al., 2011, *AJ*, 142, 72
- Evans I. N. et al., 2010, *ApJS*, 189, 37
- Fruscione A. et al., 2006, Proc. SPIE Conf. Ser. Vol. 6270, CIAO: Chandra's Data Analysis System. SPIE, Bellingham, p. 62701V
- Galeev A. A., Rosner N., Vaiana G. S., 1979, *ApJ*, 229, 318
- Gallagher S. C., Brandt W. N., Chartas G., Garmire G. P., 2002, *ApJ*, 567, 37
- Gallagher S. C., Brandt W. N., Chartas G., Priddey R., Garmire G. P., Sambruna R. M., 2006, *ApJ*, 644, 709
- Garmire G. P., Bautz M. W., Ford P. G., Nousek J. A., Ricker G. R., Jr, 2003, in Truemper J. E., Tananbaum H. D., eds, Proc. SPIE Conf. Ser. Vol. 4851, X-Ray and Gamma-Ray Telescopes and Instruments for Astronomy. SPIE, Bellingham, p. 28
- Gehrels N., 1986, *ApJ*, 303, 336
- Gibson R. R., Brandt W. N., 2012, *ApJ*, 746, 54
- Gibson R. R., Brandt W. N., Schneider D. P., 2008, *ApJ*, 685, 773
- Gibson R. R., Brandt W. N., Gallagher S. C., Schneider D. P., 2009, *ApJ*, 696, 924
- Giustini M., 2016, *Astron. Nachr.*, 337, 459
- Green A. R., McHardy I. M., Lehto H. J., 1993, *MNRAS*, 265, 664
- Green P. J. et al., 2009, *ApJ*, 690, 644
- Guo H., Shen Y., Wang S., 2018, Astrophysics Source Code Library, record [ascl:1809.008](https://ui.adsabs.org/abs/1809.008)
- Haardt F., Maraschi L., 1991, *ApJ*, 380, L51
- Jiang Y.-F., Stone J. M., Davis S. W., 2014, *ApJ*, 784, 169
- Just D. W., Brandt W. N., Shemmer O., Steffen A. T., Schneider D. P., Chartas G., Garmire G. P., 2007, *ApJ*, 665, 1004
- Kalberla P. M. W., Burton W. B., Hartmann D., Arnal E. M., Bajaja E., Morras R., Pöppel W. G. L., 2005, *A&A*, 440, 775
- Kellermann K. I., Sramek R., Schmidt M., Shaffer D. B., Green R., 1989, *AJ*, 98, 1195
- Kochanek C. S. et al., 2012, *ApJS*, 200, 8
- Kraft R. P., Burrows D. N., Nousek J. A., 1991, *ApJ*, 374, 344
- Laird E. S. et al., 2009, *ApJS*, 180, 102
- Liu H. et al., 2019, *ApJ*, 878, 79
- Livesey J., 2007, *Clin. Biochem.*, 40, 1032
- Luo B. et al., 2015, *ApJ*, 805, 122
- Lyons L., 1991, A Practical Guide to Data Analysis for Physical Science Students, Cambridge Univ. Press, Cambridge
- Maccacaro T., Gioia I. M., Wolter A., Zamorani G., Stocke J. T., 1988, *ApJ*, 326, 680
- Maronna R., Martin D., Yohai V., 2006, Robust Statistics: Theory and Methods, Wiley, New York
- McHardy I. M., Koerding E., Knigge C., Uttley P., Fender R. P., 2006, *Nature*, 444, 730
- Merloni A. et al., 2012, preprint ([arXiv:1209.3114](https://arxiv.org/abs/1209.3114))
- Middei R., Vagnetti F., Bianchi S., La Franca F., Paolillo M., Ursini F., 2017, *A&A*, 599, A82
- Miller B. P., Brandt W. N., Schneider D. P., Gibson R. R., Steffen A. T., Wu J., 2011, *ApJ*, 726, 20
- Miniutti G., Brandt W. N., Schneider D. P., Fabian A. C., Gallo L. C., Boller T., 2012, *MNRAS*, 425, 1718
- Mushotzky R. F., Done C., Pounds K. A., 1993, *ARA&A*, 31, 717
- Ni Q. et al., 2020, *ApJ*, 889, L37
- Pâris I. et al., 2012, *A&A*, 548, A66
- Pâris I. et al., 2018, *A&A*, 613, A51
- Ponti G., Papadakis I., Bianchi S., Guainazzi M., Matt G., Uttley P., Bonilla N. F., 2012, *A&A*, 542, A83
- Price-Whelan A. M. et al., 2018, *AJ*, 156, 123
- Reynolds C. S., Nowak M. A., 2003, *Phys. Rep.*, 377, 389
- Ricci C. et al., 2020, *ApJ*, 898, L1
- Richards G. T. et al., 2006, *AJ*, 131, 2766
- Richards G. T. et al., 2015, *ApJS*, 219, 39
- Rosen S. R. et al., 2016, *A&A*, 590, A1
- Saez C., Brandt W. N., Gallagher S. C., Bauer F. E., Garmire G. P., 2012, *ApJ*, 759, 42
- Schlafly E. F., Finkbeiner D. P., 2011, *ApJ*, 737, 103
- Scholz F. W., Stephens M. A., 1987, *J. Am. Stat. Assoc.*, 82, 918
- Scott A. E., Stewart G. C., Mateos S., Alexander D. M., Hutton S., Ward M. J., 2011, *MNRAS*, 417, 992
- Serafinelli R., Vagnetti F., Middei R., 2017, *A&A*, 600, A101
- Shemmer O., Brandt W. N., Paolillo M., Kaspi S., Vignali C., Lira P., Schneider D. P., 2017, *ApJ*, 848, 46
- Steffen A. T., Strateva I., Brandt W. N., Alexander D. M., Koekemoer A. M., Lehmer B. D., Schneider D. P., Vignali C., 2006, *AJ*, 131, 2826
- Strojtjohann N. L., Saxton R. D., Starling R. L. C., Esquej P., Read A. M., Evans P. A., Miniutti G., 2016, *A&A*, 592, A74
- Taylor M. B., 2005, in Shopbell P., Britton M., Ebert R., eds, ASP Conf. Ser. Vol. 347, Astronomical Data Analysis Software and Systems XIV. Astron. Soc. Pac., San Francisco, p. 29
- Taylor R. D., Uttley P., McHardy I. M., 2003, *MNRAS*, 342, L31
- Timlin J. D., Brandt W. N., Ni Q., Luo B., Pu X., Schneider D. P., Vivek M., Yi W., 2020, *MNRAS*, 492, 719
- Uttley P., McHardy I. M., Papadakis I. E., 2002, *MNRAS*, 332, 231
- Uttley P., McHardy I. M., Vaughan S., 2005, *MNRAS*, 359, 345
- Vagnetti F., Turriziani S., Trevese D., 2011, *A&A*, 536, A84
- Vagnetti F., Middei R., Antonucci M., Paolillo M., Serafinelli R., 2016, *A&A*, 593, A55
- Vaughan S., Fabian A. C., 2004, *MNRAS*, 348, 1415
- Virtanen P., et al., 2020, *Nature Methods*, 17, 261
- Watson M. G. et al., 2009, *A&A*, 493, 339
- Westfall P. H., 2014, *Am. Stat.*, 68, 191
- Weymann R. J., Morris S. L., Foltz C. B., Hewett P. C., 1991, *ApJ*, 373, 23
- White R. L., Becker R. H., Helfand D. J., Gregg M. D., 1997, *ApJ*, 475, 479
- Xue Y. Q. et al., 2011, *ApJS*, 195, 10
- York D. G. et al., 2000, *AJ*, 120, 1579
- Zhang S., Wang T.-G., Wang H., Zhou H., Dong X.-B., Wang J.-G., 2010, *ApJ*, 714, 367
- Zhu S. F., Brandt W. N., Luo B., Wu J., Xue Y. Q., Yang G., 2020, *MNRAS*, 496, 245

SUPPORTING INFORMATION

Supplementary data are available at *MNRAS* online.

Submission_table_revision1.fits

Please note: Oxford University Press is not responsible for the content or functionality of any supporting materials supplied by the authors. Any queries (other than missing material) should be directed to the corresponding author for the article.

APPENDIX A: QUASARS IN THE FULL SAMPLE

Here, we present the table containing the X-ray measurements for all of the quasars in the full sample that have multiple *Chandra* observations. A subset of the 27 total columns is reported in Table A1. The full table is available online in machine-readable format.

- (i) Column (1): Object Name.
- (ii) Column (2): J2000 Right Ascension (J2000 deg).

- (iii) Column (3): J2000 Declination (J2000 deg).
- (iv) Column (4): Redshift (see Richards et al. 2015; Pâris et al. 2018).
- (v) Column (5): Galactic column density (cm^{-2} ; Kalberla et al. 2005).
- (vi) Column (6): MJD of the *Chandra* observation (days).
- (vii) Column (7): Apparent *i*-band magnitude.
- (viii) Column (8): Reddening in the *i*-band (from the Schlafly & Finkbeiner 2011 dust map; subtract columns 7 and 8 to obtain the de-reddened *i*-band magnitude).
- (ix) Column (9): *Chandra* observation ID.
- (x) Column (10): *Chandra* off-axis angle (arcmin).
- (xi) Column (11): Full-band effective exposure time (seconds).
- (xii) Column (12): Binomial probability of detection (soft band).
- (xiii) Column (13): Binomial probability of detection (hard band).
- (xiv) Column (14): Binomial probability of detection (full band).
- (xv) Column (15)–(17): Net counts in the full band; 1σ upper and lower limits of the net full-band counts.
- (xvi) Column (18)–(19): Mean exposure map pixel value of the source and background regions ($\text{cm}^2 \text{s}$).
- (xvii) Column (20): Chip-edge flag (0 = good detection; 1 = edge detection).
- (xviii) Column (21): *Chandra* start time (s).
- (xix) Column (23): Bright cluster flag (0 = no cluster; 1 = cluster).
- (xx) Column (23): BAL flag (0 = no BAL detected; 1 = BAL present).
- (xxi) Column (24): Absolute magnitude (corrected to $z = 2$; Richards et al. 2006).
- (xxii) Column (25): Logarithm of the rest-frame monochromatic 2500 \AA luminosity ($\text{erg s}^{-1} \text{Hz}^{-1}$).
- (xxiii) Column (26): Logarithm of the rest-frame monochromatic 2500 \AA flux density ($\text{erg cm}^{-2} \text{s}^{-1} \text{Hz}^{-1}$).
- (xxiv) Column (27): Logarithm of the radio-loudness parameter, R .

Table A1. Quasars with duplicate *Chandra* observations.

Name	RA (J2000 deg)	Dec. (J2000 deg)	z	ObsID	Full.cts	TSTART (s)	BAL_flag
(1)	(2)	(3)	(4)	(9)	(15)	(21)	(23)
021000.22–100354.2	32.5009	– 10.0650	1.976	15 666	238.225	4.905E8	0
021000.22–100354.2	32.5009	– 10.0650	1.976	15 667	486.303	4.907E8	0
095732.04+024301.7	149.3835	2.7171	0.849	15 258	284.474	5.050E8	0
095732.04+024301.7	149.3835	2.7171	0.849	15 259	274.178	5.072E8	0
233722.01+002238.8	354.3417	0.3774	1.382	3248	9.930	1.425E8	0
233722.01+002238.8	354.3417	0.3774	1.382	11 728	27.384	3.669E8	0

Selected columns from the table of quasars with duplicate *Chandra* observations. Quasars without BALs present in the spectrum have a BAL_flag = 0, whereas quasars that exhibit BALs have BAL_flag = 1. Appendix A describes all of the columns in the full table. The complete table is available in machine-readable format.

This paper has been typeset from a $\text{\TeX}/\text{\LaTeX}$ file prepared by the author.